The construction mechanism of the Neoproterozoic S-type Sanfang-Yuanbaoshan granitic plutons in the Jiangnan Orogenic Belt, South China: Insights from geological observation, geochronology, AMS and Bouguer gravity modeling

Chaolei Yan, Liangshu Shu, Yan Chen, Michel Faure, Zuohai Feng, Mingguo Zhai

The construction mechanism of the Neoproterozoic S-type Sanfang-Yuanbaoshan granitic plutons in the Jiangnan Orogenic Belt, South China revealed by geological observation, geochronology, AMS and Bouguer gravity modeling

Chaolei Yan[1,2,3], Liangshu Shu[1,*], Yan Chen[2], Michel Faure[2], Zuohai Feng[4], Mingguo Zhai[3,5]

[1] *State Key Laboratory for Mineral Deposits Research, Nanjing University, 210023 Nanjing, China*

[2] *Univ. Orléans, CNRS, BRGM, ISTO, UMR 7327, F-45071, Orléans, France*

[3] *Key Laboratory of Computational Geodynamics, University of Chinese Academy of Sciences, 100049 Beijing, China*

[4] *College of Earth Sciences and Guangxi Key Laboratory of Hidden Metallic Ore Deposits Exploration, Guilin University of Technology, Guilin, 541004 Guangxi, China*

[5] *Institute of Geology and Geophysics, Chinese Academy of Sciences, 100029 Beijing, China*

Corresponding author: Liangshu Shu (lsshu@nju.edu.cn)

Abstract

The Neoproterozoic S-type granitic plutons, distributed along the suture zone of the Yangtze and Cathaysia blocks, play an important role in the tectonic evolution of the Jiangnan Orogeny. However, few researchers had focused on the scientific issues on the physical construction process of these plutons. Therefore, we carried out multidisciplinary approaches on the Sanfang and Yuanbaoshan plutons in the western Jiangan Orogenic Belt to figure out the construction mechanism of these plutons. Zircon Hf and U-Pb dating indicates that the magma, originated from the crustal partial melting, was crystallized at ca. 830 Ma. Field investigation shows that the plutons are dome shaped, and the bedding/foliation of the country rocks, the Sibao group, conform

plutons boundaries and their inclinations gradually decrease away from the contact zone. A top-to-the–E kinematic sense was observed in the eastern margin of Yuanbaoshan pluton. Both the textural analysis and AMS measurement reveal primary magmatic and secondary general top-to-the-W/NW post-solidus fabrics. The Bouguer gravity modeling reveals that the feeder zone probably locates in the southern part of each pluton and these two plutons are connected at depth. According to the primary magmatic fabric patterns, deep geometric shape as well as structural features of the country rocks, we propose that crustal partial melting magma probably intruded into the pre-existing mechanically weak (fold/fault) zone of the Sibao group, then lateral and upward accreted to construct the dome-shape plutons. The timing and mechanism of the post-solidus deformation are not well constrained, the interpretations are remain hypothetical.

Keywords: South China; Jiangnan Orogenic Belt; Neoproterozoic S-type granite; Anisotropy of magnetic susceptibility; Bouguer gravity modeling

1 Introduction

Magmatic rocks are important constituents of the continental crust and good markers for the crust evolution (Castro, 2014; de Saint-Blanquat et al., 2006; Paterson, 2009), and magmatic activity plays a significant role in the crust-mantle interaction and recycling of crustal material (Faure and Pons, 1991; Roman and Jaupart, 2016). Therefore, it is essential to study the magmatism to have a better understanding of the magmatic process and the crustal evolution. Several aspects, such as: i) magma generation, ii) differentiation, iii) transport and ascent, and iv) emplacement, must be distinguished in the magmatic evolution (Glazner and Bartley, 2006). The magma emplacement is an important stage of the process as it is the only one that can be directly investigated through field and laboratory studies. During the emplacement, some features observed both in the pluton and country rocks embody the interaction between the magma fluids and

lithosphere as well as the mechanism of space accretion during the magma emplacement (Paterson et al., 2008).

Previous studies showed that the magma intrusion are not only dominated by the physical properties (i.e., magma composition, temperature, pressure and the rheology of the crust etc.), but also controlled by syn-magmatic regional tectonic setting (Caricchi, et al., 2007; Castro, 1987; Castro et al., 2014; de Saint-Blanquat et al., 2006; Hutton, 1988; Moyen et al., 2003; Pitcher, 1979; Wei et al., 2016). Consequently, deciphering the process of magma emplacement, i.e., (1) the 3D structure of the pluton (Cruden, 1988; Mathieu et al., 2008; O'Driscoll et al., 2006; Stevenson et al., 2007); (2) granite internal fabrics (Liu et al., 2018; Tarling and Hrouda, 1993; Wei et al., 2014); (3) the magma flow pattern (Clemens and Mawer, 1992; Ernst and Baragar, 1992; Moreira et al., 2015; Paterson, 2009); (4) the thermal conditions and deformation of the granite and country rocks (Byerly et al., 2017; de Saint-Blanquat et al., 2001; Paterson et al., 1989; Žák et al., 2007), can help to understand the evolutions of the granitic pluton and the continental crust.

S-type granite is considered as produced by partial melting and crystallization of Al-rich rocks, such as orthogneiss and pelitic sedimentary rocks forming the lower to middle continental crust. It is commonly accepted that peraluminous magma is a syn- to post-orogenic product formed by the melting of the thickened orogenic root (Chappell and White, 2001). Moreover, S-type granite may emplace in a post-orogeny setting (e.g., most of the post-orogenic plutons in the Early Paleozoic orogen of SE China; Song et al., 2015; Wang et al., 2012b; Yan et al., 2017), and also in an active continental margin (Cenozoic western Pacific; Collins and Richards, 2008).

In the Jiangnan Orogenic Belt (JOB), which marks the collision belt between the Yangtze and Cathaysia blocks, the peraluminous granitic plutons sporadically crop out from east to west, such as the Shexian, Xucun, Shiershan, Jiuling, Yuanbaoshan, Sanfang, Bendong and Fanjingshan

plutons (Fig. 1). A large quantity of work on the geochronology and geochemistry suggest that these plutons are post-orogenic ones (e.g., Shu, 2012; Shu et al., 2019; Wang et al., 2013, 2014b; Yao et al., 2014a, Zhang and Wang, 2016; Zhang et al 2013).

So far, rare studies have focused on the physical construction process of the S-type granite in the JOB, however it is essential for understanding the process of the Jiangnan Orogeny. The geological observation, anisotropy of magnetic susceptibility (AMS) and gravity are efficient ways to decipher the construction process and deep geometric shape of the plutons (Liu et al., 2018). In order to obtain a better knowledge of the Neoproterozoic Jiangnan Orogeny, studies on the emplacement of the Neoproterozoic S-type granitic plutons along the JOB as well as their detailed consideration of the pluton construction, syn-magmatic and syn (post)-tectonic settings are necessary. Consequently, we choose the Sanfang-Yuanbaoshan plutons as the study targets to decipher the evolution of the Jiangnan Orogeny.

2 Geological setting

2.1 The Jiangnan Orogenic Belt (JOB)

The JOB is a key tectonic element of the South China Block, representing the Neoproterozoic NE–SW to E-W trending belt developed as a consequence of the amalgamation between the Yangtze and Cathaysia blocks. The oceanic subduction of the Paleo-South China Ocean beneath the Yangtze Block since ca. 1000 Ma (Shu et al., 2014, 2019; Wang et al., 2007; Yao et al., 2014b, 2019) was responsible for the formation of the Jiangnan magmatic arc, and followed by the collision (or continental subduction) of the Cathaysia Block after its final closure (Shu, 2012; Wang et al., 2012a). Groups of ultramafic, mafic magmatic, volcanic rocks, limestones, cherts and turbidites are interpreted as ophiolites and dated from ca. 1000 Ma to ca. 840 Ma, distributing

along the suture zone (BGMRAH, 1982; BGMRJX, 1984; BGMRZJ, 1989; Shu et al., 2015, 2019; Sun et al., 2017; Xia et al., 2018).

The Precambrian strata in the JOB are composed of the Sibao and Danzhou groups and their equivalents. The Danzhou group unconformably covers the Sibao group. The unconformity between these two groups indicates that an orogenic event took place before the sedimentation of the Danzhou group and its equivalents. This collision resulted in essentially folding and weak metamorphism (mainly under greenschist facies conditions) in the Sibao group and its equivalents (BGMRGX, 1985; BGMRHN, 1988; Charvet, 2013; Shu, 2006, 2012). The tight NE-SW to N-S striking folding and faulting are widely developed in the Sibao group and its equivalents in the whole JOB resulted by the northwestward subduction of the Paleo-South China oceanic crust and the subsequent collision of the Yangtze and Cathaysia blocks (Shu, 2012), whereas the structure of the Danzhou group was characterised by broad and gentle folds with a weak metamorphism, or even no metamorphism (BGMRGX, 1985; BGMRHN, 1988; Yao et al., 2014b).

In the JOB, the Sibao group was intruded by peraluminous granitic plutons dated at ca. 840-815 Ma with a peak of 830 Ma (e.g., Bendong, Fanjingshan, Sanfang, Shexian, Shiershan, Jiuling, Xucun and Yuanbaoshan plutons; Fig. 1; Guo et al., 1989; Shu et al., 1991, 1994, 2019; Xin et al., 2017; Yao et al., 2014b). After the formation of the original South China continent, the Nanhua intracontinental rifting developed at ca. 810 Ma–760 Ma by probably upwelling mantle magma just ending the Jiangnan Orogeny (Li et al., 2003). The NE-SW striking Nanhua rifting was coeval with the generation of bimodal igneous rocks in the Jiangnan and Cathaysia regions, including the western Yunnan, northern Guangxi, northern Hunan, northern Jiangxi, northern Zhejiang and Northern Fujian basins (Li et al., 2008; Shu et al., 2006, 2011; Wang and Li, 2003).

2.2 Sanfang-Yuanbaoshan granitic plutons and country rocks

The Sanfang and Yuanbaoshan granitic plutons are located in the western segment of the JOB (Fig. 1), and show sub a N-S elongated elliptic shape with an area of ca. 1,000 km^2 and ca. 300 km^2, respectively, and an aspect ratio about 2:1 (Fig. 2).

These two granitic plutons both intruded into the Sibao group which is mainly composed of bathyal to abyssal terrigenous arenaceous-argillaceous metasediments with bedded flysch, and chaotic turbidity deposits with olistoliths (BGMRGX, 1985; Yao et al., 2014a). Previous studies reveal that the crystallization age of these plutons ranged from 823±5 Ma to 833±6 Ma with high Aluminium Saturation Index ranging in 1.15-1.40 (Yao et al., 2014b). Their geochemical features indicate that the magma of Sanfang and Yuanbaoshan plutons were derived from supracrustal source rocks (Wang et al., 2006). The widespread occurrence of tourmaline in these plutons (Li, 1999) reveals that the granites are highly evolved and incorporated a significant amount of fluids.

As for the deformation, Li (1999) proposed that all the granitic intrusions were deformed in different degrees showing foliation with gneissic texture. Faults are developed in both plutons as well as in their country rocks (Fig. 2), mainly striking in the NE-SW and N-S directions. Some kilometer to meter- scale mafic and ultramafic blocks enclosed in the mudstone-sandstone of the Sibao group crop out around the plutons. The well folded but low greenschist-facies metamorphosed Sibao group is commonly recognized by the accretionary complex coeval with the subduction of the Paleo-South China oceanic crust (Wang et al., 2014a; Zhou et al., 2009), and recently work reveals that the upper Sibao group was deposited during the Yangtze-Cathaysia continental collision (Yan et al., 2019).

The Danzhou group unconformably covers the Sibao group, with distinct differences in the deformation style. It mainly consists of sandstone and mudstone featured by gentle folds with a low grade metamorphism, or even no metamorphism (BGMRGX, 1985).

3 Field observation and microscopic investigation

In the field, we made observations on these two plutons and their adjacent country rocks as much as possible in order to obtain maximal information on macroscopic features of rocks with a large surface covering, and figured out their geological nature.

3.1 Granitic plutons

The Sanfang and Yuanbaoshan plutons stand at a varying elevation ranging from ca. 200 to ca. 2000 meters above sea level (a.s.l.). These two porphyritic monzogranitic plutons are mainly made up of quartz, K-feldspar, plagioclase, muscovite and biotite. Tourmaline and plagioclase nodules can be observed in some outcrops where the monzogranite shows fine or coarse grain facies (Fig. 2).

It is worthy to note that these two plutons are generally undeformed in the relatively lower part though some deformation can be occasionally observed in contact zone, whereas deformed in the upper part (generally above 700 meters a.s.l.). In our visited localities, all the massive and undeformed granites are at the relatively low elevation (e.g., A51: 566m, A55: 317m, B14: 234m, B19: 329m). These undeformed granites display magmatic textures with euheral crystals of quartz, feldspars and micas (Fig. 3A and 3B). The quartz grains show a slightly undulose extinction (Fig. 4A, 4B and 4C).

However, the most deformed granites crop out in the relatively higher part (e.g., A43: 993m, A46: 983m, B08: 802m, B17: 837m).A consistent low angle (~25°) foliation is developed within the deformed granites, dipping to the W and SW. Augen structure, gneissic structure and shear

band are common in this deformed part. The mineral and stretching lineations are developed by elongated quartz grains, biotite and muscovite aggregates, and pressure shadows around the K-feldspar megacrysts trending in the E-W direction, with the top-to-the-W kinematics (Fig. 3C). Moreover, in the highly deformed granites, the quartz and muscovite are totally recrystallized and show a preferred orientation. Myrmekites develop within the K-feldspars (Fig. 4D), indicating that the granites have experienced dynamic metamorphism as the myrmekite is an exolution of quartz and plagioclase due to fluid circulation during deformation (Castle and Lindsley, 1993; Garcia et al., 1996). And mica fishes from these two granitic plutons both show the top-to-the-W or -SW kinematics (Fig. 4E and 4F).

3.2 Country rocks

The Sibao group is well exposed in the Sanfang-Yuanbaoshan area. Previous studies indicate that the Sibao group was tightly folded with general N-S and NNE-SSW striking axes (BGMRGX, 1985). However, our investigation reveals that the structural occurrence of the Sibao group is also accommodated to the shape of the pluton with generally outward dipping. The original sedimentary bedding (S_0) and foliation (S_1) with moderate to steep angle mostly strike parallel with the border of the Sanfang and Yuanbaoshan plutons (Fig. 2). Moreover, we can find that the dip angle of the $S_{0\text{-}1}$ gradually decreases as the distance away from the contact border (Fig. 3E and 3F). In our visited area, two hornfel outcrops with width of 20-30cm are found in the western and eastern contact borders between the Sanfang pluton and Sibao group (Fig. 3D). The top-to-the-downward and -outward deformations are founded in the contact zones in the northern margin of the Sanfang pluton and eastern margin of the Yuanbaoshan one (Fig. 3K).

Previous studies also revealed a greenschist facies metamorphism for the Sibao group (BGMRGX, 1985). Based on our macro-/microscopic observations, we found the degree of deformation and metamorphism of the Sibao group varies greatly in different zones.

Similar to the phenomenon of *elevation vs metamorphism and deformation* within the granitic plutons, in general, the degree of the metamorphism and deformation of the Sibao group seems gradually increases from the lower part to the higher part, the field investigation revealed that: (i) The Sibao group at the elevation below 200 meters mainly consists of sandstone and mudstone and doesn't display metamorphism neither deformation (Fig. 3E and 3F); (ii) At the elevation of ca. 200-700 meters, the degrees of the metamorphism and deformation are higher than those of below the 200 meters. In this unit, the rocks mainly consist of slate and phyllite. The foliation (S_1) transposed from the original sedimentary bedding (S_0) is rather scattily distributed, the lineations are better developed with a sub E-W direction, meanwhile the textures reveal top-to-the-W kinematics (Figs. 3G, 4G and 4H); (iii) For the Sibao group at the altitude higher than 700 meters, the degrees of deformation and metamorphism are much more developed with respect to the former lower parts. The original beddings (S_0) are well folded and even overturned as recumbent fold (S_1), with the axis gently plunging to the north (Fig. 3H). However, the later foliations S_2 consistently dip to the W with angles of 15-45°, with consistently oriented sub E-W lineations (Fig. 3I). Moreover, mylonite and ultramylonite of the Sibao group were observed at the altitude of 1000-1600 meters, with horizontal foliation and E-W directed lineation (Fig. 3J).

4 Magma crystallization age and Hafnium isotopic analysis

The magma U-Pb crystallization age and geochemical features of the Sanfang and Yuanbaoshan plutons have been investigated since the past twenty years (e.g., Li, 1999; Yao et al., 2014b). With the recent development of analysis techniques, we have collected two dating

203 samples, A37 (1403) and B13 (2024) (Figs. 2 and 7), to obtain constraints on the age of these
204 plutons.

205 **4.1 Zircon U-Pb age**

206 Heavy liquid and magnetic techniques are used for separating the zircon grains, which were
207 afterward mounted in epoxy resin, polished and coated with gold. The zircon U–Pb isotopes were
208 analyzed at the Testing Center of Shandong Bureau of China Metallurgical Geology Bureau
209 (TCSBCMGB), using a ThermoX2 ICP–MS connected to a GeoLas Pro 193 nm laser ablation
210 system. The detailed measurements and data calculation can be referred in Liu et al. (2010).

211 Cathodoluminescence (CL) images of zircons were acquired by using a JEOL JXA8230
212 electron probe microanalyzer at TCSBCMGB. Typical CL images of zircons are showed in Figure
213 5A and 5B, revealing that the grains are characterized by oscillatory zoning. Moreover, the high
214 Th/U values (0.35 in average) indicate the zircons are magmatic originated (Hoskin and
215 Schaltegger, 2003).

216 All of the U–Pb ages are listed in Table 1 and graphically displayed in Figure 5. Thirty seven
217 ages are obtained for each pluton (Sanfang and Yuanbaoshan), yielding the range of 814-1150 Ma
218 and 827-2720 Ma, respectively (Fig. 5D and 5G). However, most of the data provide ages between
219 820 to 850 Ma (Fig. 5E and 5H), with weighted mean $^{206}Pb/^{238}U$ ages of 830±2 Ma and 830±5
220 Ma, respectively (Fig. 5F and 5I). Some ages older than 2.0 Ga may indicate the existence of
221 Paleoproterozoic rocks below the plutons. These grains may be xenocrystals involved in the
222 granitic magma.

223 **4.2 Zircon Hf isotopic analysis**

224 The zircon Hf isotopic model age tells a minimum age for the material from which the zircons
225 sourced. In order to have an idea about the evolution of the zircons, we carried out the analysis on

the Zircon Hf isotopes by Neptune MC–ICP–MS at Nanjing University. For calculating the model ages of the zircons, we used the standard zircon 91500 as external sample with a $^{176}Hf/^{177}Hf$ value of 0.282300 ± 8 (2σ). During analysis, the $^{176}Lu/^{177}Hf$ of average crust is 0.015. Lu decay constant of $1.865x10^{-11}$ was applied for the calculation of the initial $^{176}Hf/^{177}Hf$ values (Scherer et al., 2001). The isotopic ratios of the $^{176}Hf/^{177}Hf$ and $^{176}Lu/^{177}Hf$ for the chondrite and depleted mantle are 0.282772 and 0.0332, 0.28325 and 0.0384, respectively (Blichert–Toft and Albarede, 1997).

About half of the U–Pb dated zircons from the Sanfang granite were selected for in–situ Hf isotopic analysis that performed where used for U–Pb dating. All of the Hf isotopic analytical results and εHf(t) versus U–Pb age diagram are presented in Table 2 and Figure 5C, respectively. The sample of A37 (1403) shows negative εHf(t) values, ranging from -1.89 to -11.15, with an average of -4.63. Correspondingly, the two-stage model ages chiefly plot on 1828–2143 Ma, while separately project at 2418 Ma (Fig. 5C). The results suggest that such granite sample was derived from some Paleoproterozoic basement rocks. Moreover, all the εHf(t) values are under the Chondritic uniform reservoir (CHUR) line, which indicates that little or no mantle component has been involved into the source rock during the partial melting and magma ascent.

5 Rock magnetic investigation and results

5.1 Field sampling

A total of 352 cores from 55 sites were sampled for the AMS study, 35 and 20 for the Sanfang and Yuanbaoshan plutons, respectively, along all possible roads with an interval of ~2 km (Fig. 7). Each site of fresh outcrop covers several tens of square meters and at least six cores are drilled with an interval of 3 to 4 meters between each other from each site.

5.2 Magnetic mineralogical analysis

In order to define the magnetic susceptibility carriers in our samples, we have carried out following methods: (1) magnetic hysteresis loop characterization by using a vibrating magnetometer in the Laboratoire de Paleomagnétisme of the Institue de Physique du Globe de Paris (IPGP); (2) isothermal remanence magnetization characterization with an IM30 pulsed magnetizer and a JR5 spinner magnetometer at the Insititut des Sciences de la Terre d'Orléans (ISTO); (3) thermomagnetic characterization using a KLY5 kappabridge coupled with a CS3 furnace at ISTO; and (4) scanning electron microscope (SEM) with the ZEISS MERLIN Compact for the minerals at ISTO.

A total of nine samples were chosen for magnetic mineralogical analysis, and the representative results are presented in Figure 6. The hysteresis curves (Fig. 6A) present similar S-shaped hysteresis loops with significant difference between the corrected and uncorrected curves, suggesting that the main magnetic susceptibility carriers could be both ferromagnetic and paramagnetic minerals. Rapid saturation of isothermal magnetic remanence at about 200 mT is featured by Sample A46 (Fig. 6B), indicating the existence of ferromagnetic minerals with low magnetic coercivity. However, for Sample A48, the gradual saturation until to 1.0 Tesla (Fig. 6B) highlights that the existence of ferromagnetic minerals with high magnetic coercivity. The rates of saturation of Samples A65 and A67 are in-between A46 and A48 (Fig. 6B), revealing both the weak and high coercive ferromagnetic minerals in the granites. The thermomagnetic measurements on Samples A10 and A23 yield a quick decrease of the magnetic susceptibility at about 580℃ (A10 in Fig. 6C) and continuous drop until to 680°C (A23 in Fig. 6C), which suggest the existence of (titano) magnetite and hematite. Moreover, these two samples show a continuous rise of magnetic susceptibility in the cooling stage (owing to oxidation reactions) revealing that a

significant mineral transformation occurred during the heating, e.g. iron sulfide to iron oxide (Fig. 6C). The SEM investigation reveals that the existence of titanomagnetite with the mass fraction of the TiO_2 ranged from 45.51% to 50.65%, and they are commonly intergrown or partly enclosed along the cleavage and boundary of biotite (Fig. 6D). The Day-plot of hysteresis parameters is presented in Figure 6E, showing that (titano) magnetite of the measured samples drop in the multidomain zone (e.g., Dunlop, 2002). It indicates that the major (elongated) axis of the magnetic susceptibility ellipsoid can be correlated to the major morphological axis of minerals (e.g., Borradaile and Henry, 1997).

Consequently, the carriers of magnetic susceptibility are composed by ferromagnetic minerals, for instance, multidomain (titano) magnetite and hematite, and of paramagnetic minerals, such as biotite, muscovite and feldspar. According to Rochette et al. (1992), the magnetic fabrics of these minerals are comparable to the petrographic ones. Therefore, the AMS measurements will be an effective way to obtain the information on the petrofabrics of granite, so that to decipher the granitic magma emplacement (Martín-Hernández et al., 2004).

5.3 AMS parameters

The measurements of AMS were performed with a KLY5 Kapprabridge at ISTO. A total of 352 (228 and 124 from the Sanfang and Yuanbaoshan, respectively) specimens with 2.5 cm in diameter and 2.2 cm in length from 55 sites were prepared. Detailed information can be found in Table 3. The mean bulk magnetic susceptibility (Km) of each sampling site from the Sanfang and Yuanbaoshan plutons varies from 27.5 to 133.0×10^{-6} SI and 32.7 to 197.0×10^{-6} SI, respectively (Fig. 8A, 8B and 8D). The site-mean value of the anisotropy degree of the magnetic susceptibility (P_J) ranges in [1.017, 1.156] and [1.009, 1.172] for the Sanfang and Yuanbaoshan plutons, respectively (Fig. 8B, 8C and 8E). The site-mean of shape parameter (T) ranges in [-0.384, 0.912]

and [-0.384, 0.817] for the Sanfang and Yuanbaoshan, respectively (Fig. 8C and 8F). No obvious correlation of P_J can be observed with Km (Fig. 8B) and elevation (Fig. 8C), however, the P_J and T are positively related (Fig. 8F). Moreover, P_J and T values both increase with the rising of elevation (Fig. 8D and 8E), which is illustrated in the cross section of Figure 8H.

5.4 AMS results

The AMS results for all sampling sites are given in Figure 7. Differences are obvious and significant between the undeformed and deformed granites according to the features of their magnetic foliation and lineation, degree of anisotropy and shape parameter (Figs. 7 and 8). In our visiting area, the undeformed granites with magmatic fabrics can be roughly partitioned as NW and SW borders, S part, and SE border of the Sanfang pluton, and SE part and NE border of the Yuanbaoshan pluton, meanwhile in order to read easily, these zones are also shown by Arabic numbers 1, 2, 4 and 6, respectively in Figure 8. In the NW and SW borders of the Sanfang pluton (Zone 1), the magnetic foliations consistently dip to the E with the inclination ranged from 33° to 79°, but the magnetic lineations span from N to S with a relative concentration on the SE dipping. Almost all the specimens show P_J value lower than 1.1 and magmatic fabrics with even shape parameters between oblate ($T>0$) and prolate ($T<0$). In the S part of the Sanfang pluton (Zone 2), the magnetic foliations mainly dip to the W with inclinations varying from 31° to 63°, and magnetic lineations span from ~230° to 330°, with a relative concentration in nearly E-W directed. 94% of the specimens have P_J values lower than 1.1 and the ratio between the oblate and prolate shapes is about 2:1. The SE border of the Sanfang pluton (Zone 4) displays the gentle magnetic foliations with dispersed magnetic lineations. All the P_J values are lower than 1.1 and the ratio of shape parameter between the oblate and prolate is about 2:1. Moreover, in the SE part and NE border of the Yuanbaoshan pluton (Zone 6), the strikes of the magnetic foliations mainly dip SW

316 with relative steep inclinations from 35° to 76°, and the magnetic lineations are essentially SSE.
317 Most of the P_J values are lower than 1.1, and the ratio between the oblate and prolate shapes is
318 about 1:1.

319 However, the deformed granites are recognized in the Central to NE Sanfang pluton and in
320 the Central to NW Yuanbaoshan pluton (Zones 3 and 5, respectively; Fig. 8). In the Central to NE
321 part of the Sanfang pluton (Zone 3), the P_J values, with the range from 1.041 to 1.187, are higher
322 than other zones in the Sanfang pluton. 37% of the specimens with the P_J value higher than 1.1,
323 suggesting that the magnetic fabric could have been modified in the post-solidus state (Tarling and
324 Hrouda, 1993). The magnetic foliations gently dip to the SW, with coherent NEE-SWW directed
325 magnetic lineations. More than 95% of the shape parameters of specimens are greater than zero,
326 i.e., oblate shape. Similarly, the Central to NW part of the Yuanbaoshan pluton (Zone 5) highlights
327 P_J values ranging from 1.017 to 1.183. 57% of sites in this zone provide P_J values higher than 1.1,
328 and almost all of these sites present positive values for shape parameter, i.e., oblate shape. They
329 show moderate magnetic foliations dipping ranging from 4° to 27°, with consistent NW-SE
330 directed magnetic lineations.

331 Consequently, the AMS results of these two plutons can be divided into two aspects, namely,
332 the magmatic fabric and tectonic one, corresponding to the undeformed and deformed granites,
333 respectively (Figs. 7 and 8). These two parts seem to be qualitatively distinguished at the
334 approximate altitude of 600-800m. To simplify the description, we utilize the average altitude line
335 of 700m as the separatrix between the undeformed and deformed granites.

336 Moreover, it is worth noting that a few samples (about less than 5 per cents) show the
337 incoherent results with respect to above description. The samples B01, B03 and B04 are in the
338 relative low elevation (~500m), but their petro/magnetic fabrics seem like a tectonic origin, with

obvious sigmoid feldspar and high P_J values ranges in [1.064, 1.079] (Fig. 7), therefore, these localities have been classified to Zone 5. Meanwhile, the samples A48, A60 and A61 are in the relative higher part, but displaying massive granite and lower P_J values ranges in [1.026, 1.042] compared to the ductilely deformed granites (Figs. 7 and 8G), hence, these localities are categorized in Zone 1. Furthermore, the two massive granite samples A33 and B11 display different magnetic features with respect to the adjacent ones, showing vertical magnetic foliations and gentle lineations which are all parallel to the boundary between the granitic plutons and country rocks (Fig. 9).

In order to have an integrated view of features of the magnetic foliations and lineations, a synthetic distribution map of magnetic foliations and lineations are presented in Figure 9. Generally, the magnetic foliations and lineations can be separated into two parts as previously documented, respectively. For the magmatic fabrics, the predominant strike of the foliation of the Sanfang and Yuanbaoshan plutons is sub N-S directed, and the secondary group is sub E-W directed. Two major groups of lineations are identified in the Sanfang pluton, namely the NEE-SWW and NNW-SSE directed ones. And the distinct magmatic lineations are sub NNW-SSE directed in the Yuanbaoshan pluton. However, for the tectonic fabrics, a set of consistent gentle SW dipping magnetic foliation and gently SWW directed magnetic lineation is recognized in the Sanfang pluton. Whereas dispersed magnetic foliations with gentle inclination are identified in the deformed granite in the Yuanbaoshan within a group of gently NW directed magnetic lineations (Fig. 9).

6 Gravity modeling

The regional gravity anomaly embodies the density heterogeneity of the underground, hence, the proper decipherment of the gravity anomaly data would help us to know the construction of

the geological bodies in the deep (Martelet et al., 2013), especially, the intrusive geological bodies usually present obvious density contrast with the wall rocks. Consequently, the gravity modeling method has been applied to deduce the Sanfang and Yuanbaoshan pluton shapes within the Sibao strata. The Bouguer gravity anomaly map for the Sanfang-Yuanbaoshan area is acquired at the China Geological Survey. The Digital Elevation Model (DEM) for the Sanfang-Yuanbaoshan area is obtained from the CGIAR-CSI database.

We collected both the granites and country rocks for the density measurements, which have been carried out at the University of Nanjing by using the Matsuhaku Electronic Densimeter GH-300. For each sample, we measured twice and took the average value at a precision of 0.001g/cm^3. Detailed density data for the samples from the granites, Sibao group, Danzhou group and Sinian strata can be referred in Table 4. As the post Sinian strata is poorly exposed, we take it as same as the density of the Sinian strata. Besides, the density of the mafic-ultramafic block is referred to the geological survey of the Guangxi province (BGMRGX, 1985). The density value of 2.670g/cm^3 for the background in the study area is referred in CRUST 1.0.

In the Bouguer gravity anomaly data, both the short and long wavelength signals are involved, which reflect the surface and deep signatures, respectively. Thus the long wavelength signals should be removed for the purpose of getting appropriate gravity anomaly information just induced by the sub-surface geological units. The Butterworth Low-Pass Filter is applied for removing the long wavelength signals with cut-off wavelengths of 10, 20, 30… to 130, 140 and 150 kilometers. Through the comparison of the residual gravity anomaly and geological maps, we found that the residual gravity anomaly with the cut-off wavelength of 130 km is the most suitable one, which matches best with ground surface features (Fig. 10).

The selected residual Bouguer gravity anomaly map shows two obvious negative anomaly centers in the central and southern parts of the Sanfang and Yuanbaoshan plutons, respectively (Fig. 10). The negative anomaly regions for these two plutons are both N-S directed, which concur the geometry of these two plutons. According to the residual Bouguer gravity anomaly data and regional tectonic features, five profiles are chosen for gravity modeling, two of them (WE1 and WE2) are perpendicular to the regional tectonic lines, and three (NS1, NS2 and NS3) are parallel with the regional structures.

Five interpreted profiles are presented in Figure 10. Their deep structures are modelled with the residual Bouguer gravity anomaly data, however, the surface contact relationship between each unit is depicted according to the field observations and geological maps (BGMRGX, 1985). According to the Bouguer gravity modeling along these profiles, we can characterize these two plutons as following: (1) Negative gravity anomalies are N-S long axis orientated within the Sibao group; (2) The roots of the granitic plutons are presented in a N-S orientated dyke shape; (3) In the E-W direction, two plutons are in a tongue shape; (4) For the Sanfang pluton, the deepest root is located in its southern part, and the depth is progressively decreased northwards with the shallowest depth of ca. 0.5-1 km in its northern part; (5) For the Yuanbaoshan one, the thickest part is situated in the central pluton; (6) The Sanfang and Yuanbaoshan plutons seem to be connected in the deep.

7 Discussion

7.1 Origin of the magma and its crystallization age

Numerous researches have studied the petrogeneses and tectonic settings of the Neoproterozoic granites in the JOB, the Neoproterozoic S-type granitic plutons in the JOB have been dated with U-Pb crystallization ages ranged from 840 to 815 Ma, peaking at ca. 830 Ma (e.g.,

Wang et al., 2006; Wu et al., 2006; Xue et al., 2010; Zhong et al., 2005). Besides, these plutons are characterised by the high Aluminium Saturation Index ranging from 1.15 to 1.40 (Yao et al., 2014b and references therein) and low initial εNd values from -4.8 to -7.6 with high enrichment in Rb, K and Th elements (Li, 1999). Thus the geochemical features indicate that the granites were sourced from supracrustal rocks (Wang et al., 2006).

In this study, several methods are carried out for deciphering the origin of the magma. Petrologically, the granite samples are K-feldspar megacryst rich (Fig. 3C). Structurally, the cathodoluminescence (CL) images (Fig. 5A and 5B) show zircons with clear oscillatory zoning, revealing the typical feature of zircons from acidic magma. Isotopically, moreover, all of the εHf(t) values are under the CHUR line (Fig. 5C), suggesting the melting of magma with little or even no mantle components. Consequently, we suggest the granites of the Sanfang and Yuanbaoshan plutons were generated by the partial melting of crustal materials, furthermore, the relatively homogeneous lithological features of these granitic plutons may suggest that the magma was derived from single component within the chamber.

Moreover, the new zircon results from the Sanfang and Yuanbaoshan granites provide the mean ages of these two plutons at 830±2 Ma and 830±5 Ma, respectively (Fig. 5F and 5I), which further indicates the magma crystallized at ca. 830 Ma. Few zircon grains give ages older than 2.0 Ga (Fig. 5G), indicating that a Paleoproterozoic basement probably exists below the upper crust in this area, and these old zircons were captured during the magma ascent. Furthermore, the Hf isotopic analyses show a group of two-stage model ages at ca. 1800–2400 Ma, which suggest the possible existence of Paleoproterozoic rocks beneath the JOB.

7.2 Acquisition of magnetic fabrics

According to macro/microscopic observations and AMS study, the surveyed areas in the Sanfang and Yuanbaoshan plutons can be divided into two fabric domains, namely, the sub-solidus (or magmatic) and post-solidus (or solid-state) ones (Figs. 8 and 9).

The magmatic domain concerns the zones with the elevation below ~700 meters a.s.l., in this domain, most of the granites are macroscopically quasi isotropic (Zones 1, 2, 4 and 6 in Fig. 8G). Meanwhile, relatively coherent, magnetic fabrics with N-S to NNE-SSW striking lineations and eastward and westward dipping foliations have been observed for the Yuanbaoshan pluton, however, relatively dispersed lineations with general E-W and N-S dipping foliations for the Sanfang pluton. The microscopic investigations show that quartz grains are euhedral with slightly undulose extinction (Fig. 4A and 4B), however, the biotite grains in the granite do not show any post-solidus deformation (Fig. 4B). These evidence suggest the granites have not suffered significant post-solidus deformation. Furthermore, 96% of the P_J values in this domain lower than 1.1, which indicates that the magnetic fabrics were probably acquired during the magma crystalization (Borradaile and Henry, 1997). Therefore, we propose that the magnetic fabrics in this domain are primary ones, i.e. without post-solidus overprint due to post-emplacement geological events. The shape parameters indicate both oblate and prolate shapes with equivalent proportion, which indicates that the magnetic foliation and lineation were almost equally developed, thus we may propose that the original magma probably flowed without significant influence of a regional tectonics (Tarling and Hrouda, 1993).

On the contrary, in the post-solidus domain (Zones 3 and 5 in Fig. 8G) at altitudes above ~700m a.s.l., the granites are foliated with augen gneissic structures and shear bands. Microscopic studies reveal that the quartz grains are mostly recrystallized as neograins with serrated boundaries,

showing the evidence of high temperature and high strain deformation. A top-to-the-W kinematics is macroscopically documented by the sigmoidal augen structure and shear bands, and microscopically by mica fish and pressure shadows. In addition, the P_J values of this zone are generally higher than 1.1, i.e., higher than those in the magmatic domain, suggesting that the magnetic fabrics were acquired after the magma cristalization. Moreover, it is worthy to note that almost all the shape parameters for the specimens in this domain are greater than zero (Fig. 8G), indicating the planar magnetic fabric is more developed than the linear magnetic one probably due to the deformation posterior to the crystallisation. Thus, the evidence above reveals that the magnetic fabrics of this domain are secondary, i.e., the synmagmatic ones are overprinted. However, the formation time of these post-solidus fabrics is not yet constrained, they might have been developed during the later stage of the magma emplacement or recrystallized during regional tectonic events that post-dated the plutons emplacement (Tarling and Hrouda, 1993). As this is out of the scope of this study, the possible hypotheses for this ductile deformation will not be discussed in detail in this text.

7.3 Mechanism of the magma emplacement and space creation

In this section, we concentrated on the lower part (primary magmatic fabrics) of the plutons and their wall rocks to decipher the magma emplacement process of the Sanfang and Yunabaoshan plutons, using our macro/micro observations, geochronological results, fabric measurements, gravity modelling as well as the previous data.

7.3.1 Sanfang pluton

The Sanfang pluton is elliptic shaped in the N-S long axis. Previous geological survey reveals that both of the granitic plutons and their country rocks are cut by the sub N-S directed faults,

473 which were probably generated in the Neoproterozoic period and reactivated in the Paleozoic or
474 in the Mesozoic (Fig. 2).

475 Our field investigation indicates that the bedding of the Sibao group close to the Sanfang
476 pluton conform the geometry of the pluton, the original sedimentary bedding (S_0) and foliation (S_1)
477 are nearly parallel with the border of the granite, suggesting a dome shaped pluton (Fig. 2).
478 Moreover, the dip angle of the S_{0-1} gradually decreases as the strata away from the contact border
479 (Fig. 3E and 3F). At the exposure level, the Sanfang pluton seems having rarely heated the country
480 rocks with no evidence for obvious thermal aureole, and hornfels have been only observed in two
481 localities in the contact boundary (Fig. 3D), with length 3~5m by width 20~30cm. This means that
482 the amount of heat was not so large and thus we can infer that the first magma injection was
483 probably in a small volume. It probably reveals that the magma injections took place though multi
484 episodic injections but with a small magma volume at each injection, which could be referred to
485 magma pulse amalgamation (Fig. 11; de Saint-Blanquat et al., 2006; Horsman et al., 2005).

486 In the NW and SW borders of the Sanfang pluton (Zone 1), the magnetic foliations dip E-
487 wards with moderate dipping angles (31-60°), whereas the magnetic lineations in this zone show
488 two direction groups, i.e., sub E-W plunging with steep angles (61-90°) in the southern part, and
489 N-S plunging with gentle angles (0-30°) in the northern part (Fig. 9). Moreover, in the southern
490 part of the Sanfang pluton (Zone 2), the foliations dipping W-wards with steep angles and mainly
491 W-dipping lineations may imply that the magma dominantly flowed quasi vertically and accreted
492 in the E-W direction. Furthermore, the magnetic foliations dip SE/SW-wards with moderate angles,
493 and the magnetic lineations generally show a sub E-W preferred orientation in the SE border of
494 the Sanfang pluton (Zone 4, Figs. 8 and 9).

From the integrated results, it is obvious that the magmatic foliations of the Sanfang pluton can be roughly distinguished as two sets, namely, the sub N-S striking (major) and sub E-W striking (minor). Meanwhile, the orientations of the magmatic lineations seem more scattered (Fig. 9).

The residual Bouguer gravity anomaly data show that the Sanfang pluton is also N-S elongated at depth, and reveal that the root of the Sanfang pluton is located in its southern part. And the interpreted profile NS1 suggests that the thickness of the Sanfang pluton decreases northwards (Fig. 10). From the unravelled profiles WE1 and WE2, moreover, the dyke shaped channels seem to be characterized in the pluton.

7.3.2 Yuanbaoshan pluton

The geometry of the Yuanbaoshan pluton is N-S elongated with an aspect ratio of 2:1. The field observation shows that the pluton geometric shape also well affects the occurrence of the country rocks of the Sibao group, i.e., the bedding of the sedimentary rocks follows the shapes of the pluton (Fig. 2). This appearance seems becoming weaker leaving away the pluton. The sigmoid quartz vein within the Sibao group locates to the east of the Yuanbaoshan pluton might be interrelated with the ductile shearing during the magma emplacement since such top-to-the-E kinematic is rarely developed in the study area except in the contact area between the eastern Yuanbaoshan pluton and its country rock (Fig. 3K). In the SE part and NE borders (Zone 6) of this pluton, the strikes of the magmatic foliations are principally NNW-SSE directed with steep and even vertical inclinations. And the magmatic lineations are mostly sub N-S directed and few NW-SE directed with gentle dipping angles (Fig. 9), suggesting that the magma might vertically ascend and mainly horizontally flow in the sub N-S direction in these parts. Moreover, two samples of B02 and B11, close to the boundary between the Yuanbaoshan pluton and Sibao strata, display

518 foliation with moderate to vertical inclination, and gentle lineations which parallel to the boundary
519 of country rocks. It may suggest that the magma probably flowed along the boundary of the country
520 rocks (Fig. 11).

521 Moreover, the residual Bouguer gravity anomaly yield that the root of the pluton is located in
522 the central to southern part (Fig. 10). Similar to the case of Sanfang pluton, the inferred profiles
523 NS2 and NS3 suggest that the thickness of pluton is slightly decreasing from south to north, and
524 the profiles WE1 and WE2 suggest that the dyke shaped channels seem alike also within the
525 Yuanbaoshan pluton.

526 **7.3.3 Construction processes of the two plutons**

527 Following observations and results may help to understand the pluton construction process:
528 1. the strata surrounding the pluton strike parallel to its border with progressive decrease of the
529 bedding inclination; 2. magnetic fabric patterns are characterised by principal sub N-S striking
530 foliation and partial sub E-W ones with relatively dispersed lineations for the Sanfang pluton and
531 sub N-S directed ones for the Yuanbaoshan pluton; 3. gravity modelling reveals a thick 'root'
532 located in the central to south part of the plutons with possible N-S directed dyke-shaped channels.

533 By integrating the above phenomena, we propose that the magma probably made its
534 upwelling into the Sibao group in the central to southern part of the plutons through dyke-shaped
535 channels, probably resulted by the pre-existing abundant and large-scale folds/faults within the
536 Sibao group, and laterally pushed the country rocks outwards. Due to probably the shape of pre-
537 existing structures, i.e. N-S oriented folds/faults, the magma dominantly flowed north-southwards
538 to construct the tongue- and/or sill-shaped plutons. Meanwhile, the granitic bodies were
539 progressively accreted in sub E-W direction to form the principal sub N-S oriented foliation.
540 Therefore, the N-S flow of magma and E-W accretion of pluton seem likely forming two dome

shaped plutons (Fig. 11). Nevertheless, the depth of emplacement is unclear and worthy for future investigation.

7.4 Tectonic implications and perspectives

S-type granitic plutons are interesting geological markers to understand the tectonic process, numerous such plutons are distributed along the JOB. However, their tectonic setting is still hotly debated in the past decade. Some scholars suggested that the peraluminous plutons were generated and made their intrusion during the amalgamation of the Yangtze and Cathaysia blocks, i.e., the syn-orogenic stage, while considering the coeval mafic rocks dated at ca. 850-830 Ma (Ding et al., 2008; Zhou et al., 2004). Nevertheless, some others hold the view that the granitic plutons were formed at the post-orogenic stage (Wang et al., 2013; 2014b; Yan et al., 2019; Zhang et al., 2013, 2016). These suggestions are, however, proposed only on the basis of the geochronological logic, without direct geological and physical evidence.

In this study, the field observations show some pluton emplacement related deformation in the country rocks, but no any evidence for a syn-magmatism regional scaled tectonic deformation. The primary magmatic fabrics in both plutons seem having been acquired in a regional tectonic free environment. Thus we propose that the crustal partial melting magma in the western Jiangnan area might be produced by the thickened crust and emplace into the Sibao group during a period of tectonic quiescence, in other words, the S-type granitic magma emplacement probably signifies the ending stage of the Jiangnan Orogeny.

However, the timing and mechanism of the top-to-the-W post-solidus deformation distinguished by the macro-/micro observations, and AMS study is still poorly studied. Two possible hypotheses are supposed, one is that the deformation occurred during the magma intrusion at ca. 830 Ma, whereas the other one is that it maybe caused by the Paleozoic or Mesozoic tectonic

events. However, the latter one is puzzled because of the regional deformation/metamorphism is not yet recognized in the Jiangnan region (Shu, 2012 and references therein). In order to solve these scientific issues, detailed field work on the regional deformation as well as the geochronology study, e.g., Ar-Ar dating, should be carried out in the further research.

8 Conclusions

Through this multidisciplinary study, the emplacement process and tectonic setting of the Neoproterozoic S-type Sanfang-Yuanbaoshan granitic plutons in the JOB can be concluded as following:

(1) The magma of the plutons sourced from the partial melting of crustal material, and crystallized at ca. 830 Ma;

(2) Magnetic/petrographic fabrics can be divided into two groups, namely, a primary sub-solidus, or magmatic, fabric developed during the pluton emplacement; and a secondary post-solidus, or solid-state, one related to a still uncertain tectonic process;

(3) The crustal partial melting magma probably intruded into the pre-existing mechanically weak (fold/fault) system in the Sibao group through dyke-shape channels, and afterwards dominantly flowed north-southwards to construct the tongue- and/or sill-shaped plutons, meanwhile, the granitic bodies were progressively accreted in sub E-W direction to form two dome shaped plutons;

(4) The intrusion of the S-type granitic magma probably occurred in a regional tectonic free environment, the emplacement probably marked the latest stage of the Jiangnan Orogeny.

Acknowledgments

We wish to express our thanks to Drs. Liu Hongsheng and Wei Wei for their help on the analyses of AMS and Bouguer gravity modeling. This study is supported by the National Key R

& D Program of China [No. 2016YFC0600202], National Natural Science Foundation of China [Nos. 41772204], Major Program of National Natural Science Foundation of China [Grant Nos. 41890834] and Natural Science Foundation of Guangxi [Grant Nos. 2019GXNSFDA245009]. We also gratefully acknowledge financial support by China Scholarship Council. Datasets related to this article can be found at *https://doi.org/10.6084/m9.figshare.11858388*.

References

BGMRAH (Bureau of Geology and Mineral Resources of Anhui Province)., 1982. Regional Geology of Anhui Province [in Chinese with English Abstract]. Geological Publishing House, Beijing, pp. 1–715.

BGMRGX (Bureau of Geology and Mineral Resources of Guangxi Province)., 1985. Regional Geology of Guangxi Autonomous Region [in Chinese with English Abstract]. Geological Publishing House, Beijing, pp. 1–853.

BGMRHN (Bureau of Geology and Mineral Resources of Hunan Province)., 1988. Regional Geology of Hunan Province [in Chinese with English Abstract]. Geological Publishing House, Beijing, pp. 6–664.

BGMRJX (Bureau of Geology and Mineral Resources Jiangxi Province)., 1984. Regional Geology of Jiangxi Province [in Chinese with English Abstract]. Geology Publishing House, Beijing, pp. 2–725.

BGMRZJ (Bureau of Geology and Mineral Resources Jiangxi Province)., 1989. Regional Geology of Jiangxi Province [in Chinese with English Abstract]. Geology Publishing House, Beijing, pp. 5–575.

Blichert–Toft, J., Albarede, F., 1997. The Lu–Hf isotope geochemistry of chondritesand the evolution of the mantle–crust system. Earth Planet. Sci. Lett. 148, 243–258. https://doi.org/10.1016/s0012-821x(97)00040-x.

Borradaile, G., Henry, B., 1997. Tectonic applications of magnetic susceptibility and its anisotropy. Earth Sci. Rev. 42 (1), 49–93. http://doi.org/10.1016/S0012–8252(96)00044–X.

Byerly, A., Tikoff, B., Kahn, M., Jicha, B., Gaschnig, R., Fayon, A.K., 2017. Internal fabrics of the Idaho batholith, USA. Lithosphere 9 (2), 283–298. http://doi.org/10.1130/L551.1.

Caricchi, L., Burlini, L., Ulmer, P., Gerya, T., Vassalli, M., Papale, P., 2007. Non–Newtonian rheology of crystal–bearing magmas and implications for magma ascent dynamics. Earth Planet. Sci. Lett. 264 (3), 402–419. https://doi.org/10.1016/j.epsl.2007.09.032.

Castle, R.O., Lindsley, D.H., 1993. An exsolution silica–pump model for the origin of myrmekite. Contrib. Miner. Petrol. 115, 58–65. https://doi.org/10.1007/BF00712978.

Castro, A., 1987. On granitoid emplacement and related structures. A review. Geologische Rundschau 76 (1), 101–124. https://doi.org/10.1007/BF01820576.

Castro, A., 2014. The off-crust origin of granite batholiths. Geosci. Front. 5, 63-75. https://doi.org/10.1016/j.gsf.2013.06.006.

Castro, A., Díaz-Alvarado, J., Fernández, C., 2014. Fractionation and incipient self-granulitization during deep-crust emplacement of Lower Ordovician Valle Fértil batholith at the Gondwana active margin of South America. Gondwana Res. 25 (2), 685-706. https://doi.org/10.1016/j.gr.2012.08.011.

Chappell, B.W., White, A.J.R., 2001. Two contrasting granite types: 25 years later. Australian J. Earth Sci. 48 (4), 489–499. https://doi.org/10.1046/j.1440-0952.2001.00882.x.

Charvet, J., 2013. The Neoproterozoic–early Paleozoic tectonic evolution of the South China Block: an overview. J. Asian Earth Sci. 74, 198–209. https://doi.org/10.1016/j.jseaes.2013.02.015.

Clemens, J.D., Mawer, C.K., 1992. Granitic magma transport by fracture propagation. Tectonophysics 204 (3–4), 339–360. https://doi.org/10.1016/0040-1951(92)90316-X.

Collins, W.J., Richards, S.W., 2008. Geodynamic significance of S-type granites in circum-Pacific orogens. Geology 36 (7), 559-562. https://doi.org/10.1130/G24658A.1.

Cruden, A.R., 1988. Deformation around a rising diapir modeled by creeping flow past a sphere. Tectonics 7 (5), 1091–1101. https://doi.org/10.1029/TC007i005p01091.

de Saint-Blanquat, M., Law, R.D., Bouchez, J.L., Morgan, S.S., 2001. Internal structure and emplacement of the Papoose Flat pluton: An integrated structural, petrographic, and magnetic susceptibility study. Geol. Soc. Am. Bull. 113, 976–995. https://doi.org/10.1130/0016-7606(2001)1132.0.CO;2.

de Saint-Blanquat, M., Habert, G., Horsman, E., Morgan, S.S., Tikoff, B., Launeau, P., Gleizes, G., 2006. Mechanisms and duration of non–tectonically assisted magma emplacement in the upper crust: the Black Mesa pluton, Henry Mountains, Utah. Tectonophysics 428 (1), 1–31. https://doi.org/10.1016/j.tecto.2006.07.014.

Ding, B.H., Shi, R.D., Zhi, X.C., Zheng, L., Chen, L., 2008. Neoproterozoic (～ 850 Ma) subduction in the Jiangnan orogen: evidence from the SHRIMP U -Pb dating of the SSZ -type ophiolite in southern Anhui Province. Acta Petrol. Miner. 27 (5), 375-388. https://doi.org/10.3969/j.issn.1000-6524.2008.05.001.

651 Dunlop, D.J., 2002. Theory and application of the Day plot (Mrs/Ms versus Hcr/Hc) 2. Application
652 to data for rocks, sediments, and soils. J. Geophys. Res. Atmos. 107 (B3), EPM5-1-15.
653 https://doi.org/10.1029/2001JB000487.
654 Ernst, R.E., Baragar, W.R.A., 1992. Evidence from magnetic fabric for the flow pattern of magma
655 in the Mackenzie giant radiating dyke swarm. Nature 356, 511-513.
656 https://doi.org/10.1038/356511a0.
657 Faure, M., Pons, J., 1991. Crustal thinning recorded by the shape of the Namurian–Westphalian
658 leucogranite in the Variscan belt of the northwest Massif Central, France. Geology 19, 730–
659 733. https://doi.org/10.1130/0091-7613(1991)0192.3.CO;2.
660 Garcia, D., Pascal, M–L., Roux, J., 1996. Hydrothermal replacement of feldspars in igneous
661 enclaves of the Velay granite and the genesis of myrmekite. Euro. J. Miner. 8, 703–711.
662 https://doi.org/10.1127/ejm/8/4/0703.
663 Glazner, A.F., Bartley, J.M., 2006. Is stoping a volumetrically significant pluton emplacement
664 process?. Geol. Soc. Am. Bull. 118 (9–10), 1185–1195.
665 Guo, L.Z., Shi, Y.S., Ma, R.S., Dong, H.G., Yang, S.F., 1989. The pre–Devonian tectonic patterns
666 and evolution of south China. J. Southeast Asian Earth Sci. 3, 87–93.
667 https://doi.org/10.1016/0743-9547(89)90012-3.
668 Horsman, E., Tikoff, B., Morgan, S., 2005. Emplacement-related fabric and multiple sheets in the
669 Maiden Creek sill, Henry Mountains, Utah, USA. J. Struct. Geol. 27 (8), 1426–1444.
670 https://doi.org/10.1016/j.jsg.2005.03.003.
671 Hoskin, P.W.O., Schaltegger, U., 2003. The composition of zircon and igneous and metamorphic
672 petrogenesis. Rev. Miner. Geochem. 53 (1), 27–62. https://doi.org/10.2113/0530027.

673 Hutton, D.H.W., 1988. Granite emplacement mechanisms and tectonic controls: inferences from
674 deformation studies. Earth and Environmental Science Transactions of the Royal Society of
675 Edinburgh 79, 245–255. https://doi.org/10.1017/S0263593300014255.
676 Li, X.H., 1999. U–Pb zircon ages of granites from the southern margin of the Yangtze block:
677 timing of Neoproterozoic Jinning: orogeny in SE China and implications for Rodinia
678 assembly. Precambrian Res. 97 (1), 43–57. https://doi.org/10.1016/S0301-9268(99)00020-0.
679 Li, X.H., Li, Z.X., Ge, W.C., Zhou, H.W., Li, W.X., Liu, Y., Wingate, M., 2003. Neoproterozoic
680 granitoids in South China: crustal melting above a mantle plume at ca. 825 Ma? Precambrian
681 Res. 122, 45–83. https://doi.org/10.1016/S0301-9268(02)00207-3.
682 Li, Z.X., Bogdanova, S.V., Collins, A.S., Davidson, A., De Waele, B., Ernst, R.E., Fitzsimons,
683 I.C.W., Fuck, R.A., Gladkochub, D.P., Jacobs, J., Karlstrom, K.E., Lu, S., Natapov, L.M.,
684 Pease, V., Pisarevsky, S.A., Thrane, K., Vernikovsky, V., 2008. Assembly, configuration,
685 and break–up history of Rodinia: A synthesis. Precambrian Res. 160, 179–210.
686 https://doi.org/10.1016/j.precamres.2007.04.021.
687 Liu, H., Martelet, G., Wang, B., Erdmann, S., Chen, Y., Faure, M., Huang, F.F., Scaillet, B., Breton,
688 N., Shu, L.S., Wang, R.C., Zhu, J.C., 2018. Incremental Emplacement of the Late Jurassic
689 Midcrustal, Lopolith-Like Qitianling Pluton, South China, Revealed by AMS and Bouguer
690 Gravity Data. J. Geophys. Res. Solid Earth 123, 9249-9268.
691 https://doi.org/10.1029/2018JB015761.
692 Liu, Y.S., Gao, S., Hu, Z.C., Gao, C.G., Zong, K.Q., Wang, D.B., 2010. Continental and oceanic
693 crust recycling–induced melt–peridotite interactions in the trans–North China orogen: U–Pb
694 dating, Hf isotopes and trace elements in zircons from mantle xenoliths. J. Petrol. 51, 537–
695 571. https://doi.org/10.1093/petrology/egp082.

696 Martelet, G., Perrin, J., Truffert, C., Deparis, J., 2013. Fast mapping of magnetic basement depth,
697 structure and nature using aeromagnetic and gravity data: combined methods and their
698 application in the Paris Basin. Geophys. Prosp. 61 (4), 857–873.
699 https://doi.org/10.1111/1365–2478.12024.
700 Martín-Hernández, F., Lüneburg, C. M., Aubourg, C., Jackson, M., 2004. Magnetic fabric:
701 methods and applications—an introduction. Geol. Soc. London 238 (1), 1–7.
702 https://doi.org/10.1144/GSL.SP.2004.238.01.01.
703 Mathieu, L., De Vries, B.V.W., Holohan, E.P., Troll, V.R., 2008. Dykes, cups, saucers and sills:
704 Analogue experiments on magma intrusion into brittle rocks. Earth Planet. Sci. Lett. 271 (1),
705 1–13. https://doi.org/10.1016/j.epsl.2008.02.020.
706 Moreira, M.A., Geoffroy, L., Pozzi, J.P., 2015. Magma flow pattern in dykes of the Azores
707 revealed by anisotropy of magnetic susceptibility. J. Geophys. Res. Solid Earth 120, 662-690.
708 https://doi.org/ 10.1002/2014JB010982.
709 Moyen, J.F., Martin, H., Jayananda, M., Auvray, B., 2003. Late Archaean granites: a typology
710 based on the Dharwar Craton (India). Precambrian Res. 127 (1), 103–123.
711 https://doi.org/10.1016/s0301-9268(03)00183-9.
712 O'Driscoll, B., Troll, V.R., Reavy, R.J., Turner, P., 2006. The Great Eucrite intrusion of
713 Ardnamurchan, Scotland: Reevaluating the ring–dike concept. Geology 34 (3), 189–192.
714 https://doi.org/10.1130/G22294.1.
715 Paterson S.R., Vernon R.H., Tobisch O.T., 1989. A review of criteria for the identification of
716 magmatic and tectonic foliations in granitoids. J. Struct. Geol. 11 (3), 349–363.
717 https://doi.org/10.1016/0191-8141(89)90074-6.

718 Paterson, S.R., Pignotta, G.S., Farris, D., Memeti, V., Miller, R. B., Vernon, R. H., Žák, J., 2008.
719 Is stoping a volumetrically significant pluton emplacement process?: Discussion. Geol. Soc.
720 Am. Bull. 120 (7–8), 1075–1079. https://doi.org/10.1130/B26148.1.
721 Paterson, S.R., 2009. Magmatic tubes, pipes, troughs, diapirs, and plumes: Late–stage convective
722 instabilities resulting in compositional diversity and permeable networks in crystal–rich
723 magmas of the Tuolumne batholith, Sierra Nevada, California. Geosphere 5 (6), 496–527.
724 https://doi.org/10.1130/GES00214.1.
725 Pitcher, W.S., 1979. The nature, ascent and emplacement of granitic magmas. J. Geol. Soc. 136,
726 627–662.
727 Rochette, P., Jackson, M., Aubourg, C., 1992. Rock magnetism and the interpretation of anisotropy
728 of magnetic susceptibility. Rev. Geophys. 30, 209–226. https://doi.org/10.1029/92rg00733.
729 Roman, A., Jaupart, C., 2016. The fate of mafic and ultramafic intrusions in the continental crust.
730 Earth Planet. Sci. Lett. 453, 131-140. https://doi.org/10.1016/j.epsl.2016.07.048.
731 Scherer, E., Munker, C., Mezger, K., 2001. Calibration of the Lutetium–Hafnium clock. Science
732 293, 683–687. https://doi.org/10.1126/science.1061372.
733 Shu, L.S., 2006. Pre–Devonian tectonic evolution of South China: from Cathaysia Block to
734 Caledonian period folded Orogenic Belt. Geol. J. China Uni. (Earth Sci.) 12 (4), 418–431 [in
735 Chinese with English abstract].
736 Shu, L.S., 2012. An analysis of principal features of tectonic evolution in South China Block. Geol.
737 Bull. China 31 (7), 1035–1053 [in Chinese with English abstract].
738 https://doi.org/10.1007/s11783-011-0280-z.

739 Shu, L.S., Charvet, J., Shi, Y.S., Faure, M., Cluzel, D., Guo, L.Z., 1991. Structural analysis of the
740 Nanchang-Wanzai sinistral ductile shear zone (Jiangnan region, South China). J. Southeast
741 Asian Earth Sci. 6 (1), 13-23. https://doi.org/10.1016/0743-9547(91)90091-B.
742 Shu, L.S., Zhou, G.Q., Shi, Y.S., Yin, J., 1994. Study on the high pressure metamorphic blueschist
743 and its Late Proterozoic age in the Eastern Jiangnan belt. Chinese Sci. Bull. 39, 1200–1204.
744 https://doi.org/CNKI:SUN:JXTW.0.1994-14-012.
745 Shu, L.S., Faure, M., Jiang, S.Y., Yang, Q., Wang, Y.J., 2006. SHRIMP zircon U–Pb age, litho
746 and biostratigraphic analyses of the Huaiyu Domain in South China—Evidence for a
747 Neoproterozoic orogen, not Late Paleozoic–Early Mesozoic collision. Episodes 29 (4), 244–
748 252. https://doi.org/10.1007/s00254-006-0521-9.
749 Shu, L.S., Faure, M., Yu, J.H., Jahn, B.M., 2011. Geochronological and geochemical features of
750 the Cathaysia block (South China): New evidence for the Neoproterozoic breakup of Rodinia.
751 Precambrian Res. 187 (3–4), 263–276. https://doi.org/10.1016/j.precamres.2011.03.003.
752 Shu, L.S., Jahn, B.M., Charvet, J., Santosh, M., Wang, B., Xu, X.S., Jiang, S.Y., 2014. Early
753 Paleozoic depositional environment and intracontinental orogeny in the Cathaysia Block
754 (South China): implications from stratigraphic, structural, geochemical and geochronologic
755 evidence. Am. J. Sci. 314 (1), 154–186. https://doi.org/10.2475/01.2014.05.
756 Shu, L.S., Wang, B., Cawood, P.A., Santosh, M., Xu, Z.Q., (2015). Early Paleozoic and Early
757 Mesozoic intraplate tectonic and magmatic events in the Cathaysia Block, South China.
758 Tectonics 34, 1600-1621. https://doi.org/10.1002/2015tc003835.
759 Shu, L.S., Wang, J.Q., Yao, J.L., 2019. Tectonic evolution of the eastern Jiangnan region, South
760 China: New findings and implications on the assembly of the Rodinia supercontinent.
761 Precambrian Res. 322, 42-65. https://doi.org/ 10.1016/j.precamres.2018.12.007.

762 Song, M.J., Shu, L.S., Santosh, M., Li, J.Y., 2015. Late Early Paleozoic and Early Mesozoic
763 intracontinental orogeny in the South China Craton: Geochronological and geochemical
764 evidence. Lithos 232, 360–374. https://doi.org/10.1016/j.lithos.2015.06.019.
765 Stevenson, C.T., Owens, W.H., Hutton, D.H., Hood, D.N., Meighan, I.G., 2007. Laccolithic, as
766 opposed to cauldron subsidence, emplacement of the Eastern Mourne pluton, N. Ireland:
767 evidence from anisotropy of magnetic susceptibility. J. Geol. Soc. 164 (1), 99–110.
768 https://doi.org/10.1144/0016076492006-008.
769 Sun, J.J., Shu, L.S., Santosh, M., Wang, L.S., 2017. Neoproterozoic tectonic evolution of the
770 Jiuling terrane in the central Jiangnan orogenic belt (South China): Constraints from
771 magmatic suites. Precambrian Res. 302, 279-297.
772 https://doi.org/10.1016/j.precamres.2017.10.003.
773 Tarling, D., Hrouda, F., 1993. Magnetic anisotropy of rocks. Springer Science & Business Media.
774 Wang, J., Li, Z.X., 2003. History of Neoproterozoic rift basins in South China: implications for
775 Rodinia break–up. Precambrian Res. 122, 141–158. https://doi.org/10.1016/S0301-
776 9268(02)00209-7.
777 Wang, W., Zhou, M.F., Yan, D.P., Li, J.W., 2012. Depositional age, provenance, and tectonic
778 setting of the Neoproterozoic sibao group, southeastern Yangtze block, South
779 China. Precambrian Res. 192 (1), 107–124. https://doi.org/10.1016/j.precamres.2011.10.010.
780 Wang, X.L., Zhou, J.C., Qiu, J.S., Zhang, W.L., Liu, X.M., Zhang, G.L., 2006. LA–ICP–MS U–
781 Pb zircon geochronology of the Neoproterozoic igneous rocks from Northern Guangxi, South
782 China: implications for petrogenesis and tectonic evolution. Precambrian Res. 145 (1–2),
783 111–130. https://doi.org/10.1016/j.precamres.2005.11.014.

784 Wang, X.L., Zhou, J.C., Griffin, W.L., Wang, R.C., Qiu, J.S., O'Reilly, S.Y., Xu, X.S., Liu, X.M.,
785 Zhang, G.L., 2007. Detrital zircon geochronology of Precambrian basement sequences in the
786 Jiangnan orogen: dating the assembly of the Yangtze and Cathaysia Blocks. Precambrian
787 Res. 159 (1–2), 117–131. https://doi.org/10.1016/j.precamres.2007.06.005.
788 Wang, X.L., Zhou, J.C., Griffin, W.L., Zhao, G.C., Yu, J.H., Qiu, J.S., Zhang, Y.J., Xing, G.F.,
789 2014a. Geochemical zonation across a Neoproterozoic orogenic belt: Isotopic evidence from
790 granitoids and metasedimentary rocks of the Jiangnan orogen, China. Precambrian Res. 242,
791 154-171. https://doi.org/10.1016/j.precamres.2013.12.023.
792 Wang, Y.J., Wu, C.M., Zhang, A.M., Fan, W.M., Zhang, Y.H., Zhang, Y.Z., Peng, T.P., Ying,
793 C.Q., 2012b. Kwangsian and Indosinian reworking of the eastern South China Block:
794 constraints on zircon U–Pb geochronology and metamorphism of amphibolites and
795 granulites. Lithos 150, 227-242. https://doi.org/10.1016/j.lithos.2012.04.022.
796 Wang, Y.J., Zhang, A.M., Cawood, P.A., Fan, W.M., Xu, J.F., Zhang, G.W., Zhang, Y.Z., 2013.
797 Geochronological, geochemical and Nd–Hf–Os isotopic finger printing of an early
798 Neoproterozoic arc-back-arc system in South China and its accretionary assembly along the
799 margin of Rodinia. Precambrian Res. 231, 343–371.
800 https://doi.org/10.1016/j.precamres.2013.03.020.
801 Wang, Y.J., Zhang, Y.Z., Fan, W.M., Geng, H.Y., Zou, H.P., Bi, X.W., 2014b. Early
802 Neoproterozoic accretionary assemblage in the Cathaysia block: geochronological, Lu–Hf
803 isotopic and geochemical evidence from granitoid gneisses. Precambrian Res. 249, 144–161.
804 https://doi.org/10.1016/j.precamres.2014.05.003.
805 Wei, W., Chen, Y., Faure, M., Shi, Y.H., Martelet, G., Hou, Q.L., Lin, W., Breton, N., Wang, Q.C.,
806 2014. A multidisciplinary study on the emplacement mechanism of the Qingyang–Jiuhua

massif in southeast China and its tectonic bearings. Part I: Structural geology, AMS and paleomagnetism. J. Asian Earth Sci. 86, 76–93. https://doi.org/10.1016/j.jseaes.2013.06.003.

Wei, W., Chen, Y., Faure, M., Martelet, G., Lin, W., Wang, Q. C., Yan, Q.R., Hou, Q.L., 2016. An early extensional event of the South China Block during the Late Mesozoic recorded by the emplacement of the Late Jurassic syntectonic Hengshan composite granitic massif (Hunan, SE China). Tectonophysics 672–673, 50–67. https://doi.org/10.1016/j.tecto.2016.01.028.

Wu, R.X., Zheng, Y.F., Wu, Y.B., Zhao, Z.F., Zhang, S.B., Liu, X.M., Wu, F.Y., 2006. Reworking of juvenile crust: Element and isotope evidence from Neoproterozoic granodiorite in South China. Precambrian Res. 146, 179–212. https://doi.org/10.1016/j.precamres.2006.01.012.

Xia, Y., Xu, X.S., Niu, Y.L., Liu, L., 2018. Neoproterozoic amalgamation between Yangtze and Cathaysia blocks: The magmatism in various tectonic settings and continent–arc–continent collision. Precambrian Res. 309, 56–87. https://doi.org/10.1016/j.precamres.2017.02.020.

Xin, Y., Li, J., Dong, S., Zhang, Y., Wang, W., Sun, H., 2017. Neoproterozoic post–collisional extension of the central Jiangnan Orogen: Geochemical, geochronological, and Lu–Hf isotopic constraints from the ca. 820–800 Ma magmatic rocks. Precambrian Res. 294, 91–110. https://doi.org/10.1016/j.precamres.2017.03.018.

Xue, H.M., Ma, F., Song, Y.Q., Xie, Y.P., 2010. Geochronology and geochemisty of the Neoproterozoic granitoid association from eastern segment of the Jiangnan orogen, China: Constraints on the timing and process of amalgamation between the Yangtze and Cathaysia blocks [in Chinese with English abstract]. Acta Geologica Sinica 26, 3215–3244.

Yan, C.L., Shu, L.S., Faure, M., Chen, Y., Li, C., 2017. Early Paleozoic intracontinental orogeny in the Yunkai domain, South China Block: New insights from field observations, zircon U–

Pb geochronological and geochemical investigations. Lithos 268-271, 320–333. https://doi.org/10.1016/j.lithos.2016.11.013.

Yan, C.L., Shu, L.S., Faure, M., Chen, Y., Huang, R.B., 2019. Time constraints on the closure of the Paleo-South China Ocean and the Neoproterozoic assembly of the Yangtze and Cathaysia blocks: Insight from new detrital zircon analyses. Gondwana Res. 73, 175-189. https://doi.org/10.1016/j.gr.2019.03.018.

Yao, J.L., Shu, L.S., M. Santosh, Zhao, G.C., 2014a. Neoproterozoic arc–related mafic–ultramafic rocks and syn–collision granite from the western segment of the Jiangnan Orogen, South China: Constraints on the Neoproterozoic assembly of the Yangtze and Cathaysia Blocks. Precambrian Res. 243, 39–62. https://doi.org/10.1016/j.precamres.2013.12.027.

Yao, J.L, Shu, L.S., Santosh, M., Zhao, G.C., 2014b. Neoproterozoic arc–trench system and breakup of the South China Craton: Constraints from N–MORB type and arc–related mafic rocks, and anorogenic granite in the Jiangnan orogenic belt. Precambrian Res. 247, 187–207. https://doi.org/10.1016/j.precamres.2014.04.008.

Yao, J.L, Cawood, P.A., Shu, L.S., Zhao, G.C., 2019. Jiangnan Orogen, South China: A ~970–820 Ma Rodinia margin accretionary belt. Earth Sci. Rev. 196, 102872. https://doi.org/10.1016/j.earscirev.2019.05.016.

Žák, J., Paterson, S.R., Memeti, V., 2007. Four magmatic fabrics in the Tuolumne batholith, central Sierra Nevada, California (USA): implications for interpreting fabric patterns in plutons and evolution of magma chambers in the upper crust. Geol. Soc. Am. Bull. 119 (1–2), 184–201. https://doi.org/10.1130/B25773.1.

Zhang, Y.Z., Wang, Y.J., Geng, H.Y., Zhang, Y.H., Fan, W.M., Zhong, H., 2013. Early Neoproterozoic (~850 Ma) back-arc basin in the Central Jiangnan Orogen (Eastern South

China): geochronological and petrogenetic constraints from meta-basalts. Precambrian Res. 231, 325–342. https://doi.org/10.1016/j.precamres.2013.03.016.

Zhang, Y.Z., Wang, Y.J., 2016. Early Neoproterozoic (~840 Ma) arc magmatism: geochronological and geochemical constraints on the meta-basites in the Central Jiangnan orogenic belt. Precambrian Res. 275, 1–17. https://doi.org/10.1016/j.precamres.2015.11.006.

Zhong, Y.F., Ma, C.Q., She, Z.B., Lin, G.C., Xu, H.J., Wang, R.J., Yang, K.G., Liu, Q., 2005. SHRIMP U–Pb zircon geochronology of the Jiuling granitic complex batholith in Jiangxi Province [in Chinese with English abstract]. Earth Science–Journal of China University of Geosciences, 30, 685–591.

Zhou, J.C., Wang, X.L., Qiu, J.S., Gao, J.F., 2004. Geochemistry of meso– and Neoproterozoic mafic–ultramafic rocks from northern Guangxi, China: arc or plume magmatism?. Geochem. J. 38 (2), 139–152.

Zhou, J.C., Wang, X.L., Qiu, J.S., 2009. Geochronology of Neoproterozoic mafic rocks and sandstones from northeastern Guizhou, South China: Coeval arc magmatism and sedimentation. Precambrian Res. 170, 27–42. https://doi.org/10.1016/j.precamres.2008.11.002.

Figure captions

Figure 1. Simplified tectonic map of the South China Block.

Figure 2. Geological sketch map of the Sanfang-Yuanbaoshan area with a NW-SE cross-section. For the cross-section, the contact relationship between each geological unit is depicted according to the field observations, however, the deep structure of the profile is inferred from the gravity modeling. Note that the vertical scale is exaggerated in order to show more details.

Figure 3. Representative field photos in the Sanfang-Yuanbaoshan area, with the geographic localities in the sketch map. (A) Massive granite in the Sanfang pluton; (B) Massive granite in the Yuanbaoshan pluton; (C) Foliated porphyritic granite with the top-to-the-W kinematics; (D) Hornfel between the Sanfang pluton and Sibao group; (E) Sibao group with vertical beddings; (F) Sibao group with moderate inclination; (G) Sigmoid quartz vein indicates a top-to-the-W kinematic; (H) Recumbent folding of the Sibao group, with the axis gently plunging to the north; (I) E-W directed lineations in the Sibao group; (J) Mylonite on the roof of the Yuanbaoshan pluton; (K) Eastward kinematics in the Sibao group.

Figure 4. Microphotographs with the representative features of the granites and country rocks in the Sanfang-Yuanbaoshan area. (A and B) Microphotographs of undeformed granites with crossed polarized light; (C) Undeformed granite in the Yuanbaoshan pluton; (D) Highly deformed granites showing orientated quartz and interstitial myrmekite, crossed polarized light; (E) Mica fish in the highly deformed granites showing top-to-the-W kinematics, crossed polarized light; (F) Deformed granite in the Yuanbaoshan pluton; (G) Microphotographs in reflected light of the Sibao group with top-to-the-W kinematics; (H) Sigma structure and pressure shadows in the Sibao group with top-to-the-W kinematics, crossed polarized light.

Figure 5. The Cathodoluminescence, U-Pb ages and epsilon Hf(t) results of the granite samples of A37 and B13 from the Sanfang and Yuanbaoshan plutons, respectively. (A and B) Cathodoluminescence (CL) images of zircons from two samples, with analyzed locations and U–Pb ages; (C) Plot of epsilon Hf(t) versus U–Pb age of zircons from the Sanfang pluton; (D) U–Pb concordia plots for the zircons from Sanfang granite; (E)

899 Enlarged interval of the concentrated ages in the D; (F) The average of the ages showed
900 in the E; (G) U–Pb concordia plots for the zircons from Yuanbaoshan granite; (H)
901 Enlarged interval of the concentrated ages in the G; (I) The average of the ages showed
902 in the H.

903 Figure 6. Magnetic mineralogic analyse of the granites in the Sanfang pluton. (A) Hysteresis loop
904 diagrams; (B) Acquisition of isothermal remanent magnetization (IRM); (C)
905 Thermomagnetic curves; (D) Scanning Electron Microscope imagines of the biotite
906 grains; (E) Day-plot of hysteresis parameters. Abbreviation: Magnetic coercivity of the
907 measured sample (Hc); Coercivity of magnetic remanence (Hcr); Multidomain (MD);
908 Saturation intensity of magnetic remanence (Mrs); Saturation intensity of induced
909 magnetization (Ms); Pseudo-Single-Domain (PSD); Single-Domain (SD).

910 Figure 7. Sketch map with the sampling sites and AMS results for each site.

911 Figure 8. Magnetic parameters of the granites of the Sanfang-Yuanbaoshan plutons. (A)
912 Distribution of the Km; (B) Scatter plot of the Km versus PJ; (C) Scatter plot of the Km
913 versus elevation; (D) Scatter plot of the PJ and elevation with a positive correlation; (E)
914 Scatter plot of the T and elevation with a positive correlation; (F) Scatter plot of the T
915 and PJ with a positive correlation. All the data are site-mean value for each sampling
916 site; (G) Partition of the two plutons according to the integrated criteria of field
917 observations, features of the magnetic foliations and lineations and PJ values; (H) A
918 sampling section showing generally positive correlation between the PJ value and
919 elevation. Abbreviation: Bulk magnetic susceptibility (Km); Anisotropy degree of the
920 magnetic susceptibility (PJ); Shape parameter (T).

Figure 9. A synthetic distribution map of the magnetic foliations and lineations in the Sanfang and Yuanbaoshan granitic plutons. The black symbols represent the sub-solidus fabrics, whereas the white ones correspond to post-solidus fabrics.

Figure 10. The residual Bouguer gravity anomaly map of the Sanfang-Yuanbaoshan area with five interpreted profiles.

Figure 11. 3-D model for the emplacement mechanism of the Sanfang and Yuanbaoshan plutons in ca. 830 Ma ago.

Figures

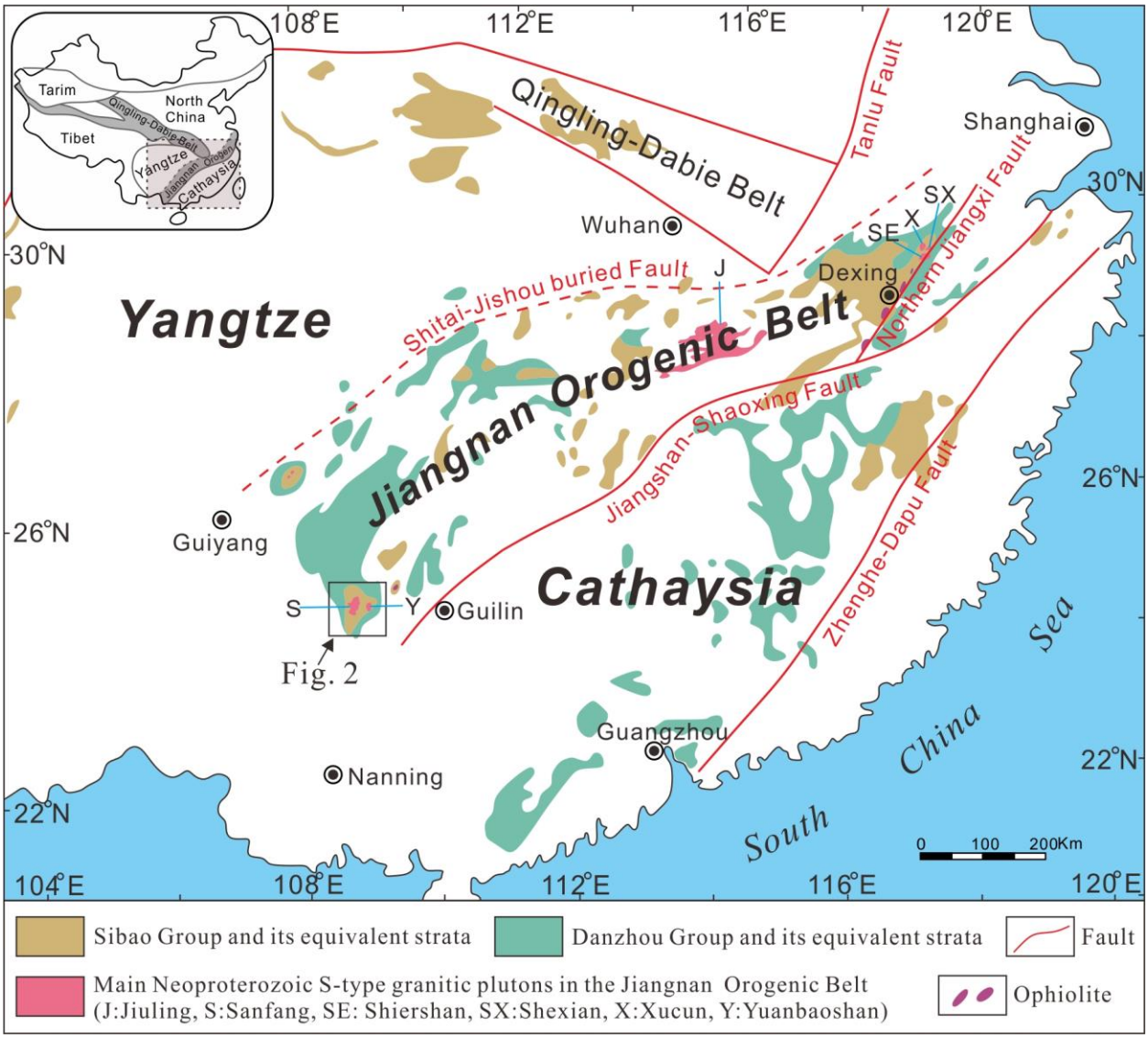

930 Figure 1

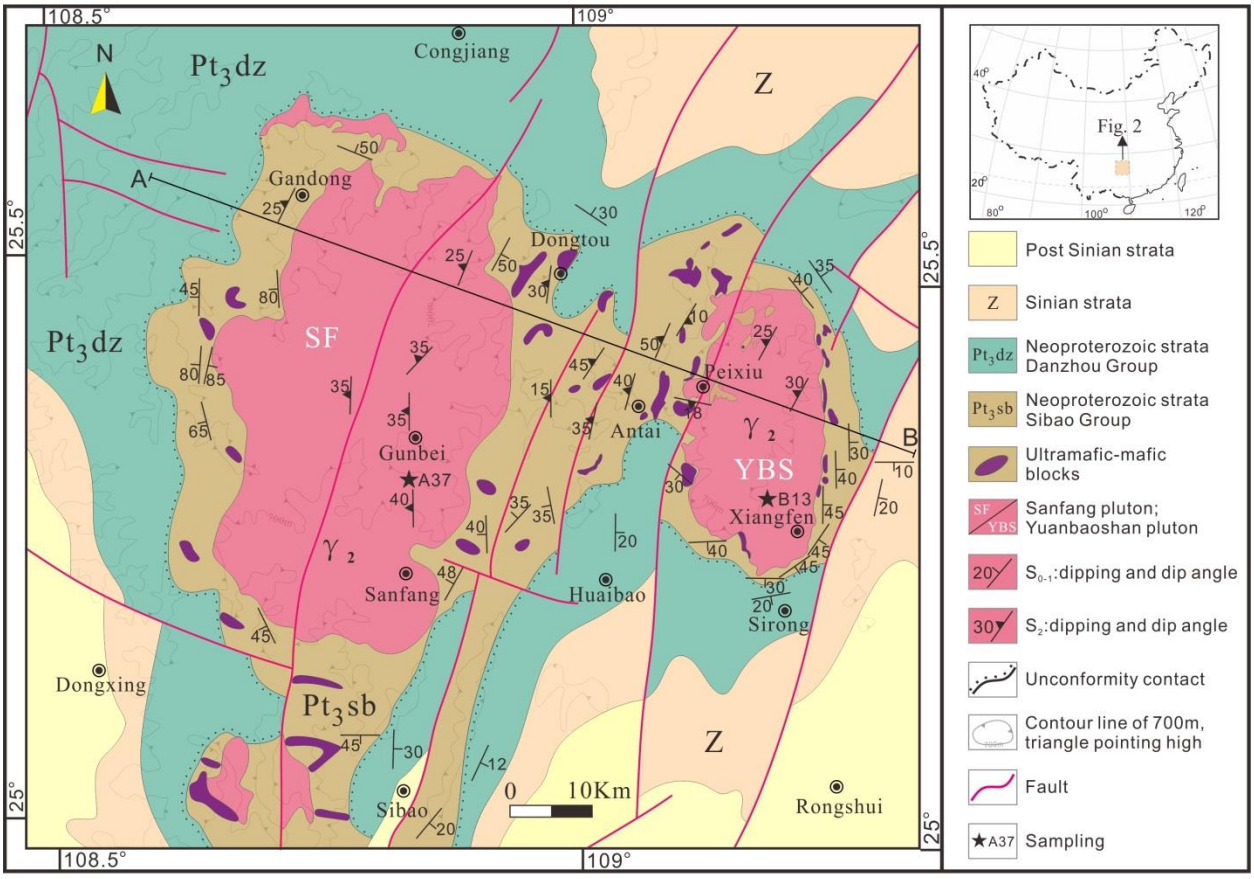

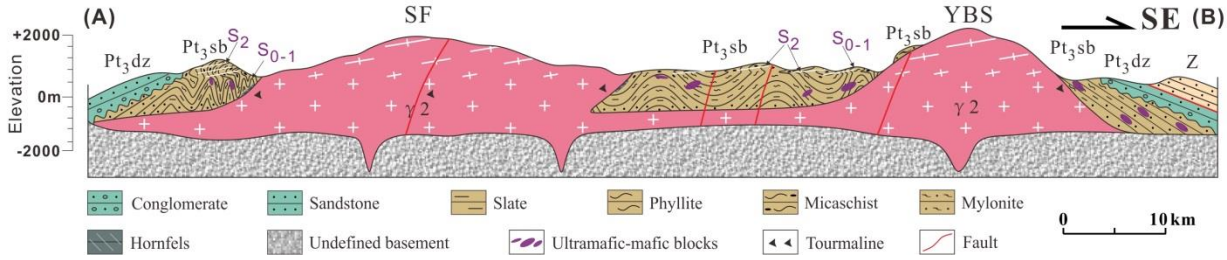

931

932 Figure 2

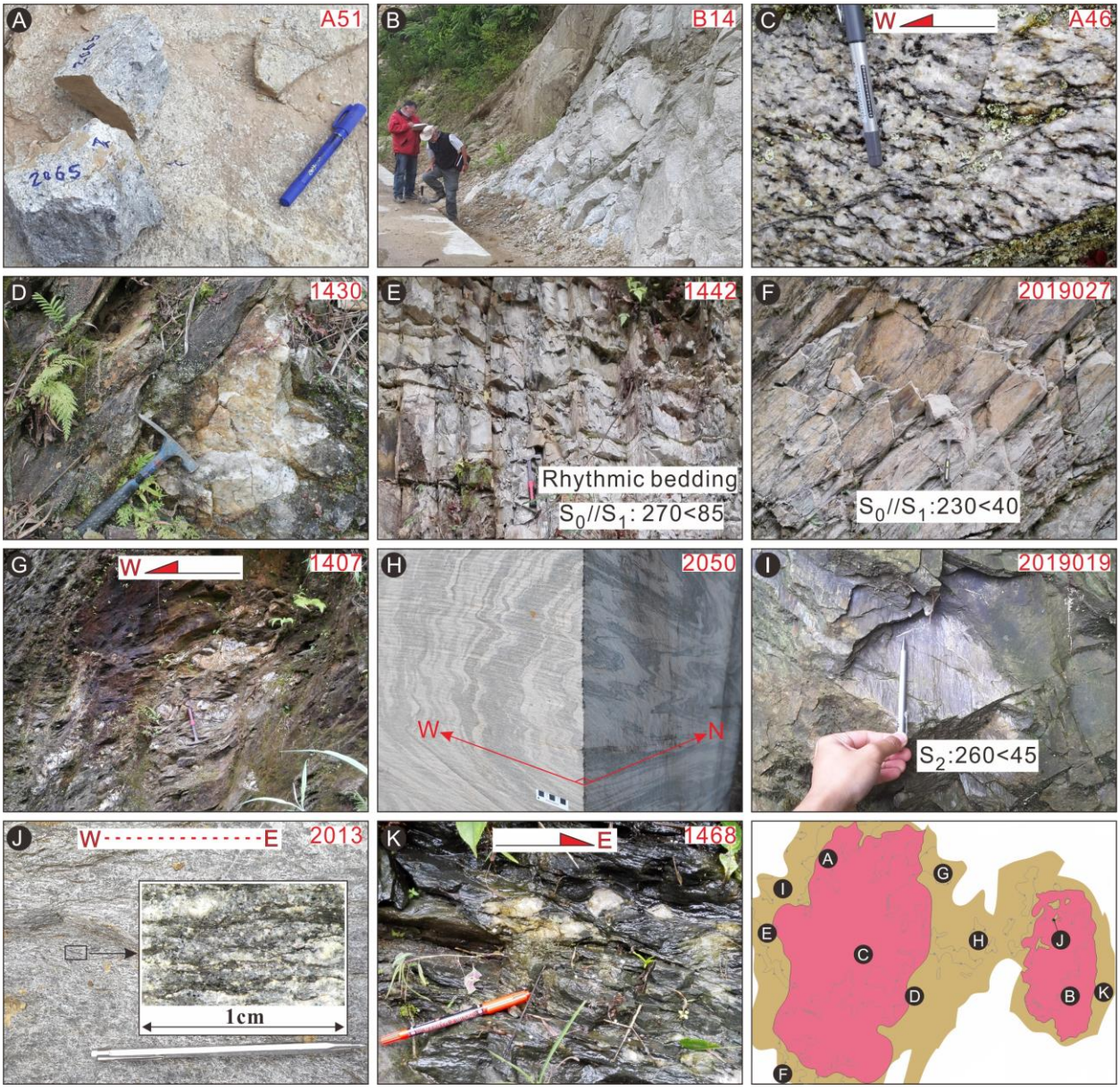

933

934 Figure 3

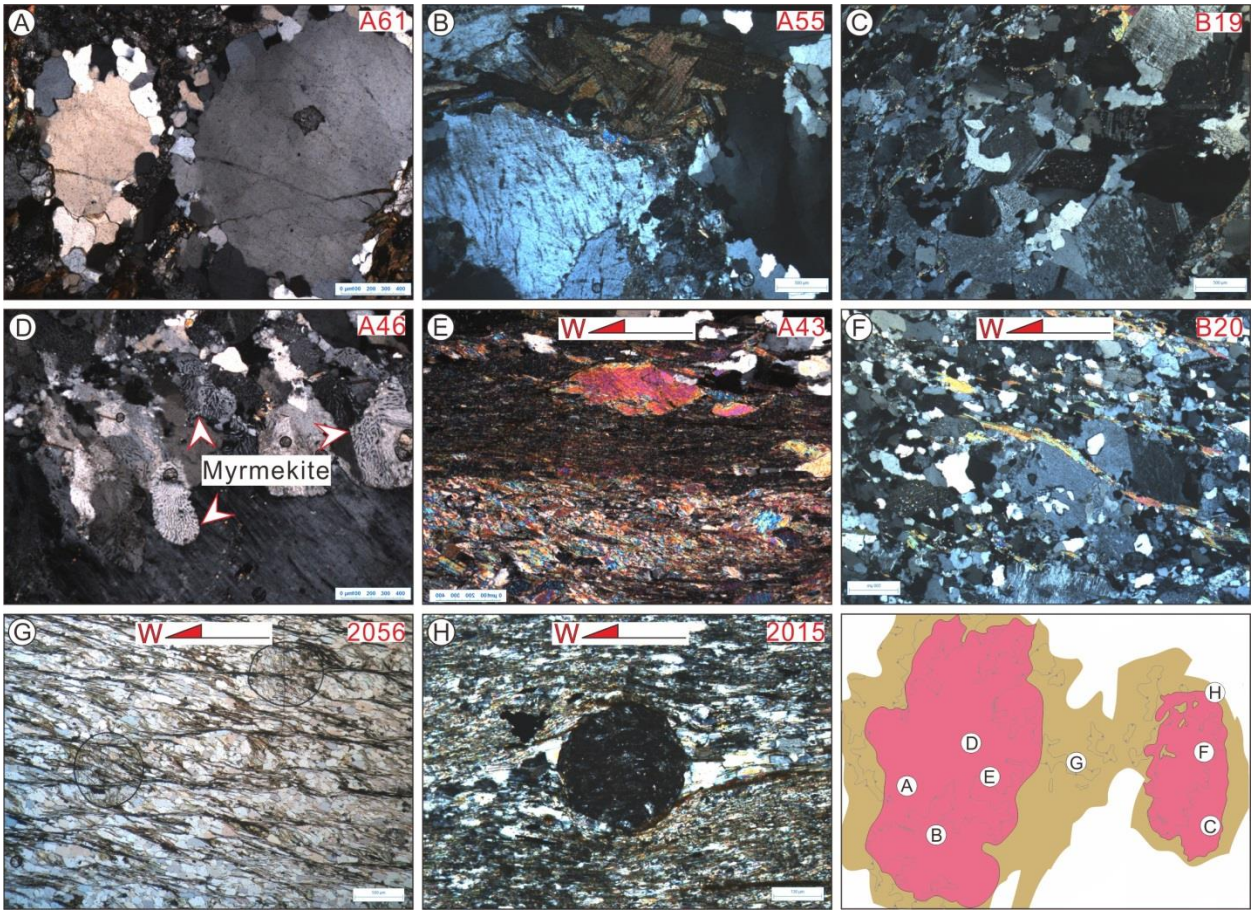
A
A61
B
A55
C
B19
D
A46
Myrmekite
E
W
A43
F
W
B20
G
W
2056
H
W
2015
H
D
F
G
E
A
C
B

Figure 4

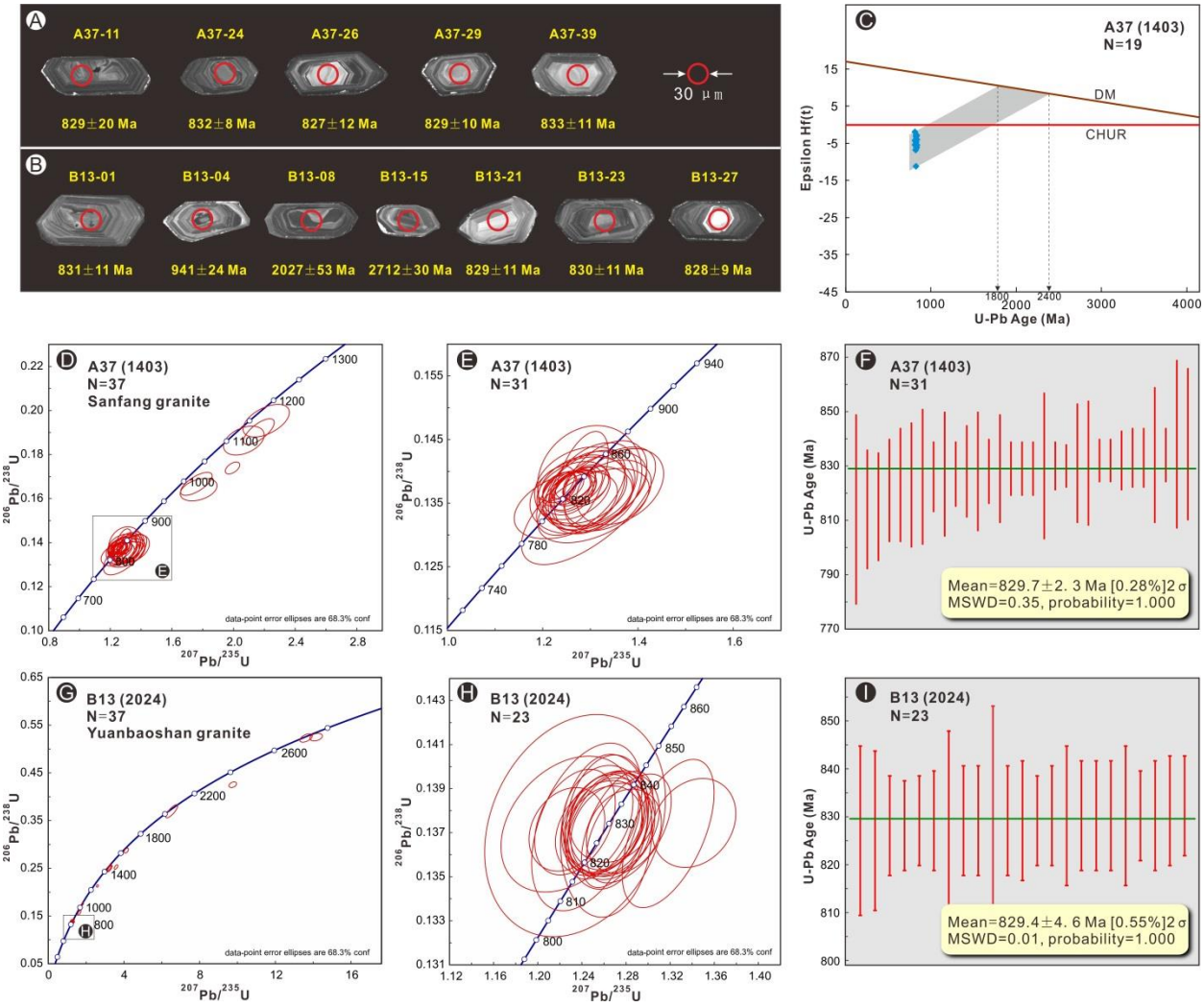
A
A37-11
A37-24
A37-26
A37-29
A37-39
829±20 Ma
832±8 Ma
827±12 Ma
829±10 Ma
833±11 Ma
30 μm
B
B13-01
B13-04
B13-08
B13-15
B13-21
B13-23
B13-27
831±11 Ma
941±24 Ma
2027±53 Ma
2712±30 Ma
829±11 Ma
830±11 Ma
828±9 Ma
C
A37 (1403)
N=19
DM
CHUR
Epsilon Hf(t)
U-Pb Age (Ma)
D
A37 (1403)
N=37
Sanfang granite
E
A37 (1403)
N=31
F
A37 (1403)
N=31
Mean=829.7±2. 3 Ma [0.28%]2σ
MSWD=0.35, probability=1.000
G
B13 (2024)
N=37
Yuanbaoshan granite
H
B13 (2024)
N=23
I
B13 (2024)
N=23
Mean=829.4±4. 6 Ma [0.55%]2σ
MSWD=0.01, probability=1.000
data-point error ellipses are 68.3% conf
$^{206}Pb/^{238}U$
$^{207}Pb/^{235}U$
U-Pb Age (Ma)

Figure 5

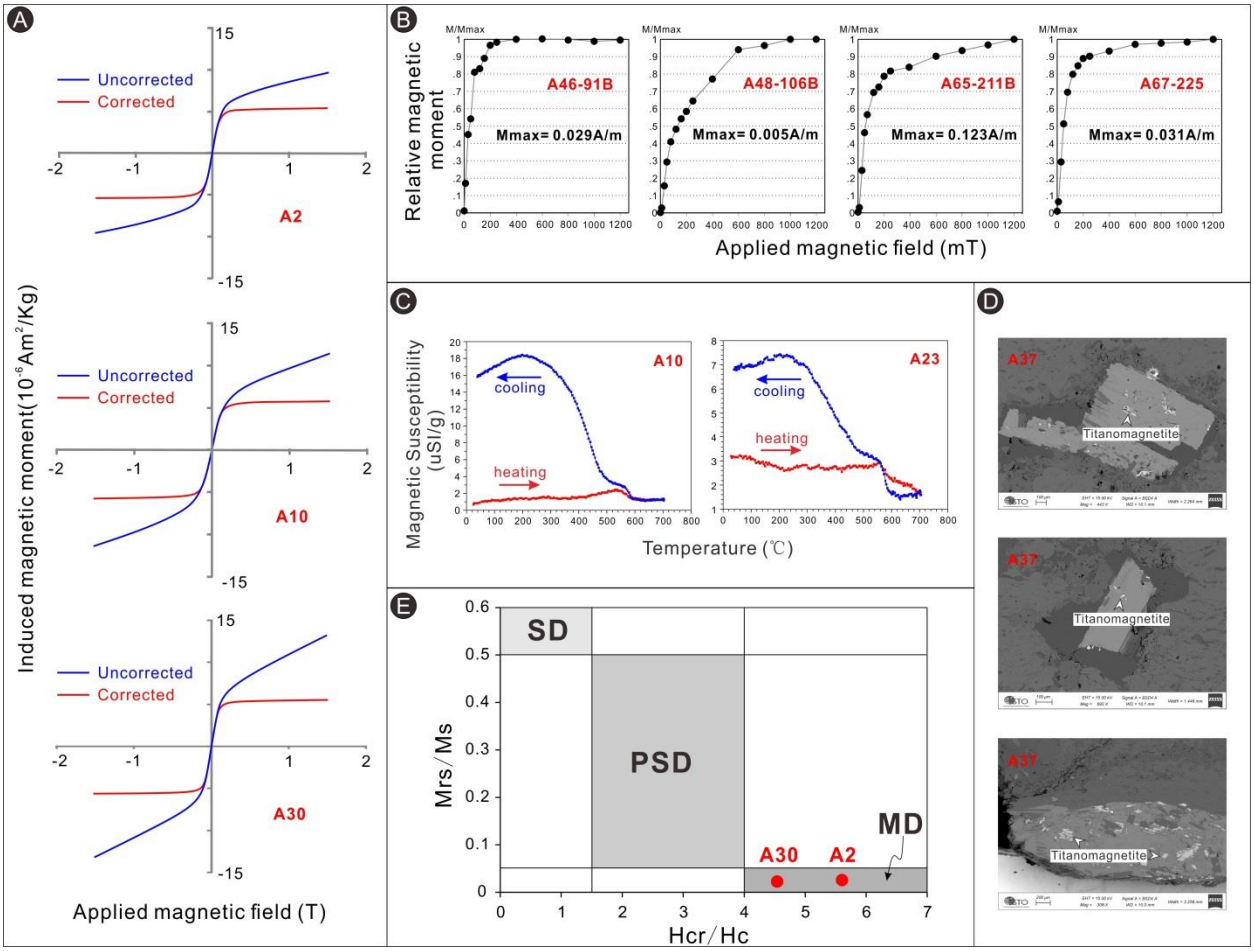
A
Uncorrected
Corrected
A2
A10
A30
Induced magnetic moment(10⁻⁶Am²/Kg)
Applied magnetic field (T)
B
Relative magnetic moment
M/Mmax
A46-91B
Mmax= 0.029A/m
A48-106B
Mmax= 0.005A/m
A65-211B
Mmax= 0.123A/m
A67-225
Mmax= 0.031A/m
Applied magnetic field (mT)
C
Magnetic Susceptibility (uSI/g)
A10
A23
cooling
heating
Temperature (℃)
D
A37
Titanomagnetite
E
SD
PSD
MD
A30
A2
Mrs/Ms
Hcr/Hc

Figure 6

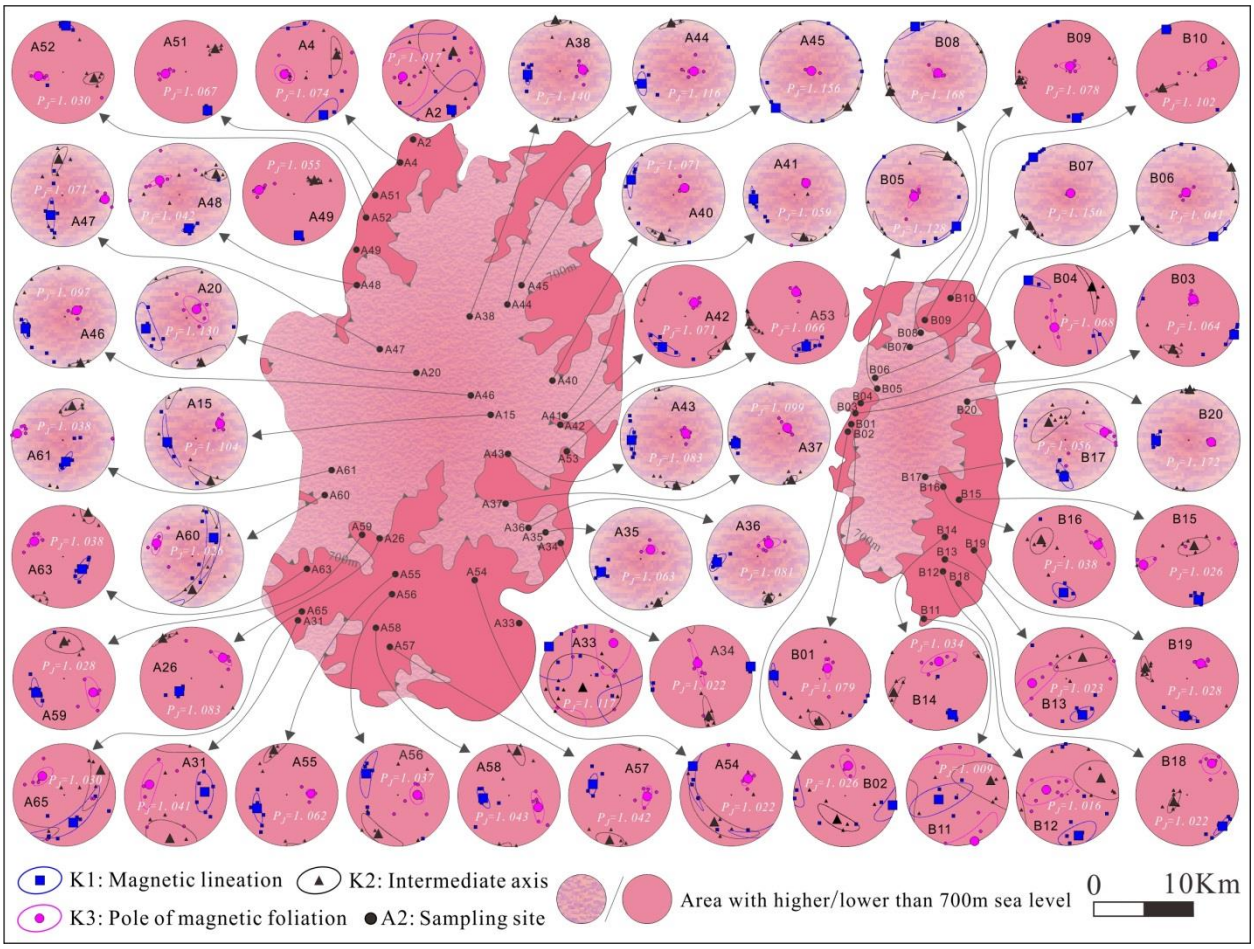

941

942 Figure 7

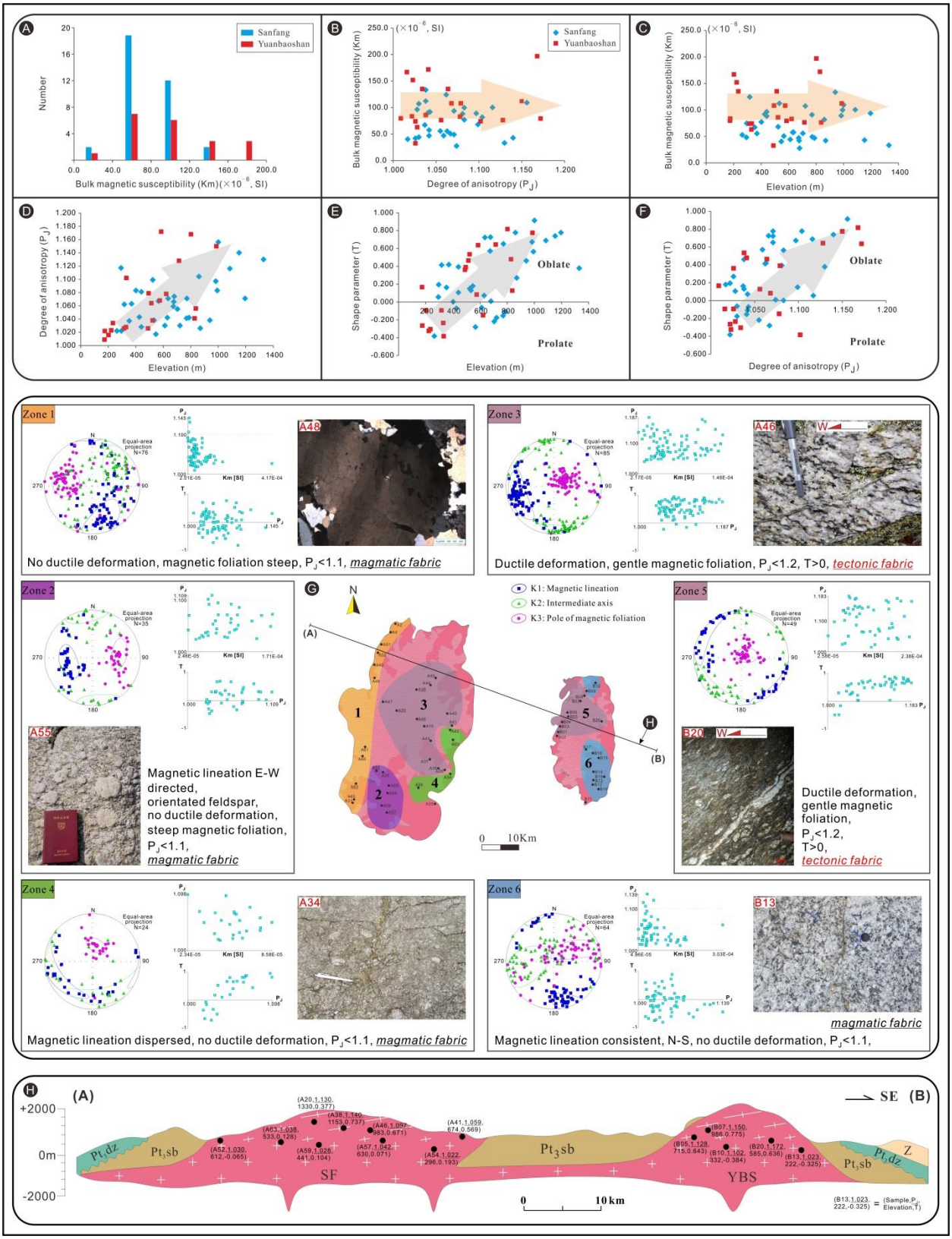

943

944 Figure 8

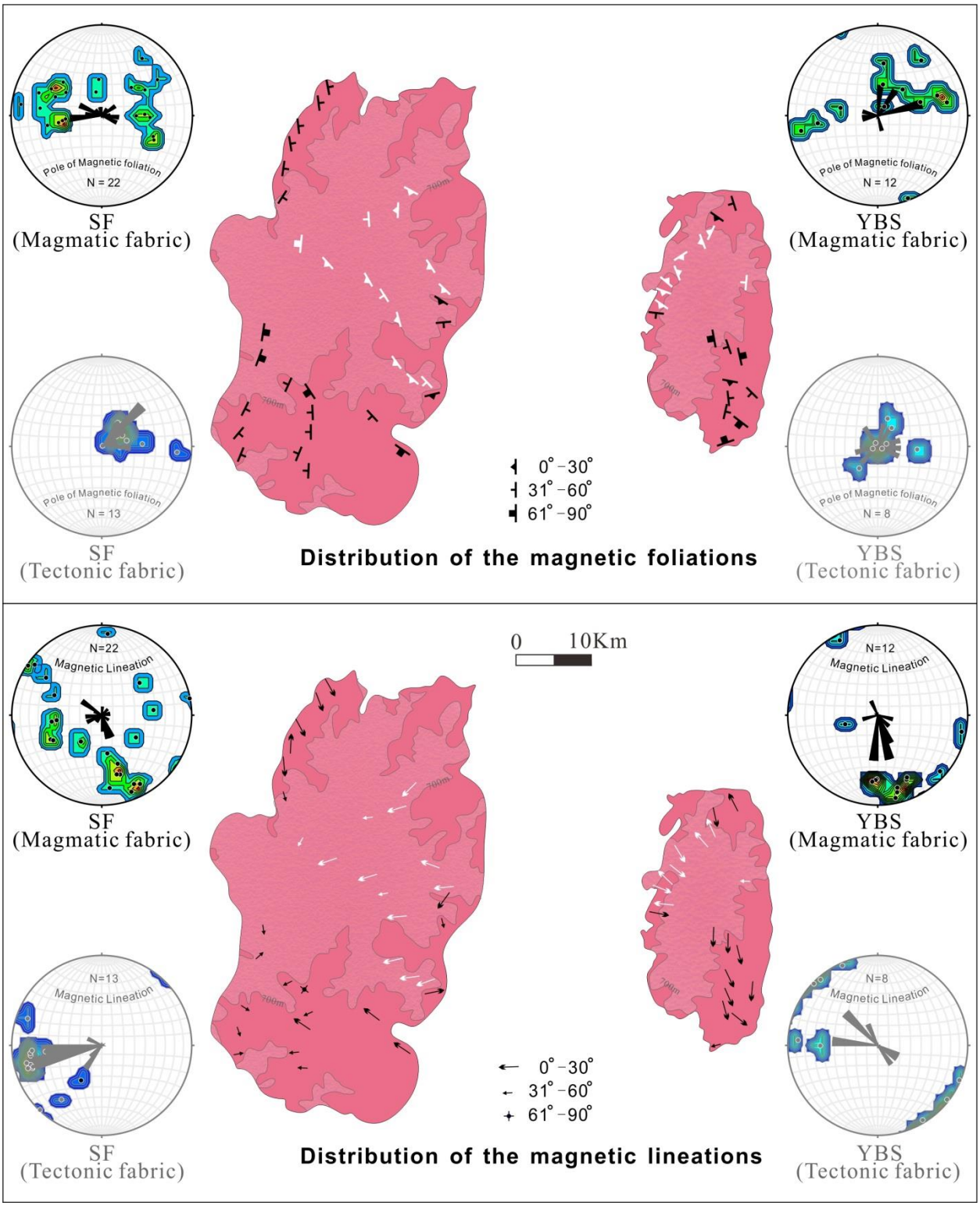
Pole of Magnetic foliation
N = 22
SF
(Magmatic fabric)
Pole of Magnetic foliation
N = 12
YBS
(Magmatic fabric)
Pole of Magnetic foliation
N = 13
SF
(Tectonic fabric)
Pole of Magnetic foliation
N = 8
YBS
(Tectonic fabric)
0°-30°
31°-60°
61°-90°
Distribution of the magnetic foliations
0 10Km
N=22
Magnetic Lineation
SF
(Magmatic fabric)
N=12
Magnetic Lineation
YBS
(Magmatic fabric)
N=13
Magnetic Lineation
SF
(Tectonic fabric)
N=8
Magnetic Lineation
YBS
(Tectonic fabric)
0°-30°
31°-60°
61°-90°
Distribution of the magnetic lineations

Figure 9

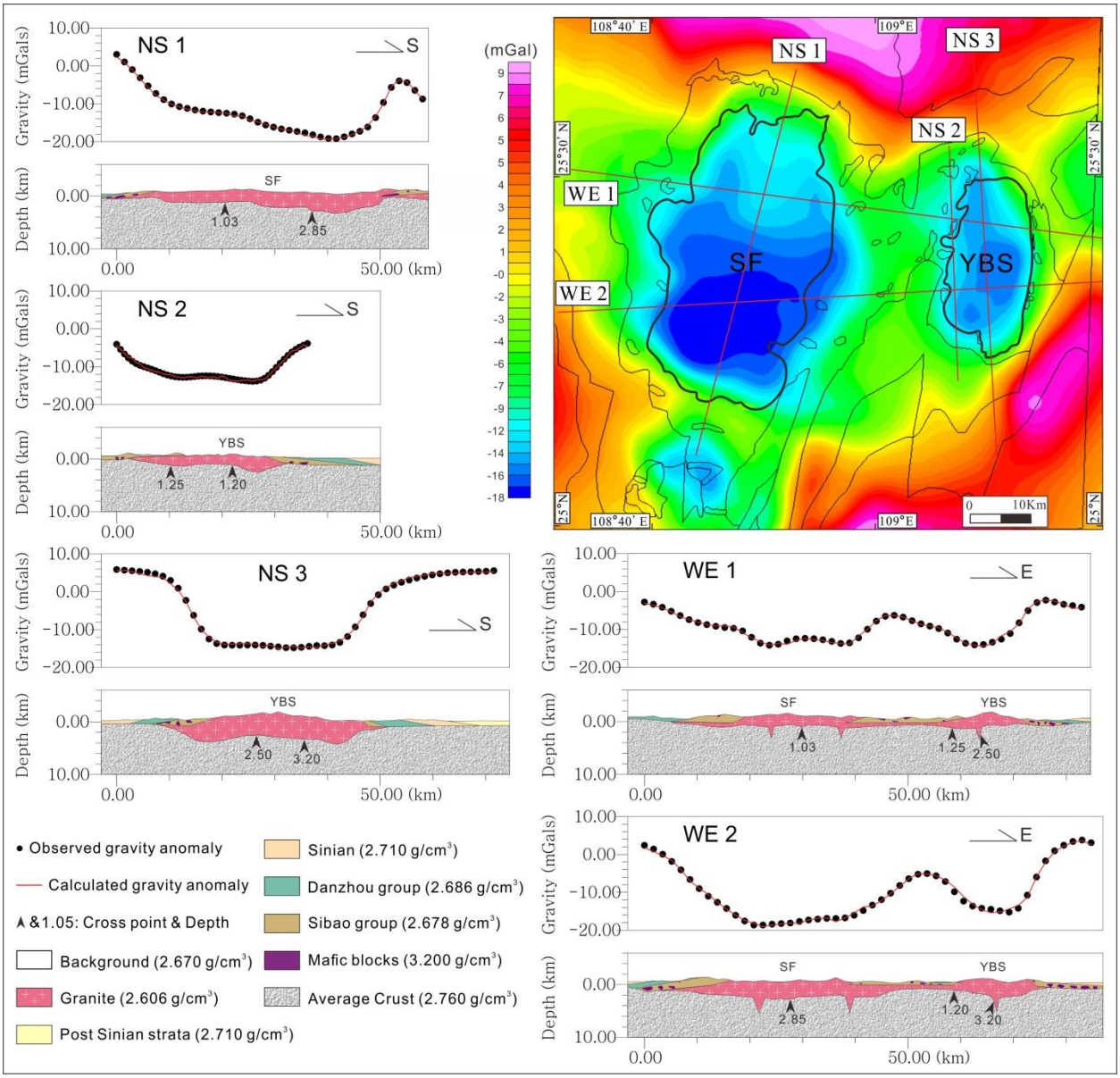
NS 1
S
Gravity (mGals)
Depth (km)
SF
1.03
2.85
0.00
50.00 (km)
NS 2
YBS
1.25
1.20
NS 3
2.50
3.20
WE 1
E
WE 2
(mGal)
108°40' E
109°E
25°30' N
25°N
0
10Km
• Observed gravity anomaly
Calculated gravity anomaly
&1.05: Cross point & Depth
Background (2.670 g/cm³)
Granite (2.606 g/cm³)
Post Sinian strata (2.710 g/cm³)
Sinian (2.710 g/cm³)
Danzhou group (2.686 g/cm³)
Sibao group (2.678 g/cm³)
Mafic blocks (3.200 g/cm³)
Average Crust (2.760 g/cm³)

Figure 10

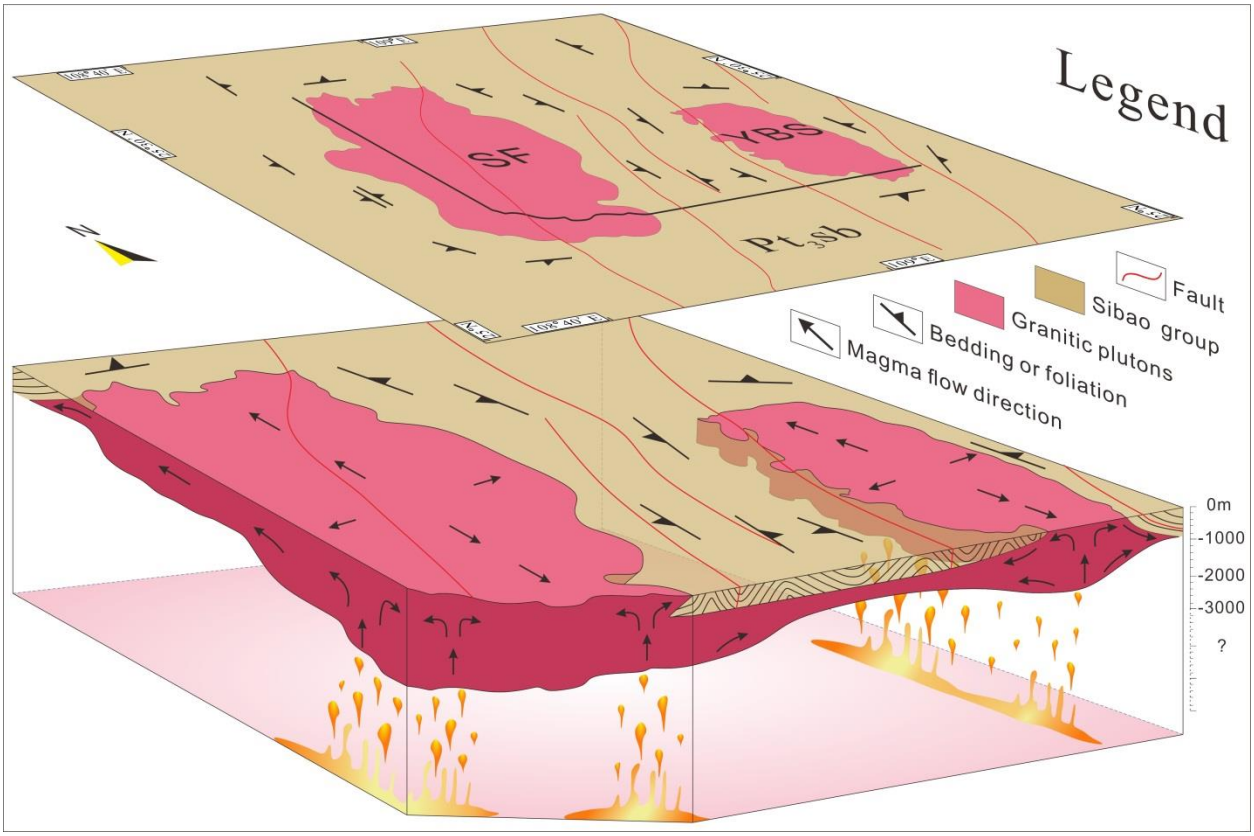
Legend
Fault
Sibao group
Granitic plutons
Bedding or foliation
Magma flow direction
SF
YBS
Pt3Sb
N
0m
-1000
-2000
-3000
?

Figure 11

Tables

Table 1. LA-ICP-MS zircon U-Pb dating results for the granite samples from the Sanfang and Yuanbaoshan plutons

Analysis	*CORRECTED RATIOS*						*CORRECTED AGES (Ma)*							
	207Pb/206Pb	*1σ*	*207Pb/235U*	*1σ*	*206Pb/238U*	*1σ*	*207Pb/206Pb*	*1σ*	*207Pb/235U*	*1σ*	*206Pb/238U*	*1σ*	*concordance*	*Th/U ratios*
Sample A37 (1403)														
1403-1	0.064170	0.003370	1.248450	0.071490	0.134730	0.003510	747	114	823	32	815	20	99%	0.94
1403-2	0.066760	0.003550	1.296120	0.092800	0.134580	0.006090	830	114	844	41	814	35	96%	0.24
1403-3	0.067440	0.003490	1.306550	0.077200	0.134610	0.003850	851	110	849	34	814	22	95%	0.27
1403-4	0.075440	0.003150	1.773600	0.078940	0.164030	0.003350	1080	86	1036	29	979	19	94%	0.15
1403-5	0.068760	0.002930	1.337000	0.059900	0.136220	0.003670	892	90	862	26	823	21	95%	0.37
1403-6	0.079070	0.003050	2.212030	0.099380	0.195370	0.004880	1174	78	1185	31	1150	26	97%	0.56
1403-7	0.065360	0.002550	1.264680	0.050930	0.136980	0.003010	786	84	830	23	828	17	99%	0.43
1403-9	0.078520	0.003100	2.067010	0.087200	0.186330	0.004330	1160	80	1138	29	1101	24	96%	0.40
1403-10	0.067610	0.003180	1.294370	0.061930	0.135810	0.003290	856	100	843	27	821	19	97%	0.43
1403-11	0.066860	0.003240	1.283580	0.061330	0.137200	0.003550	833	103	838	27	829	20	98%	0.05
1403-12	0.067490	0.003790	1.281600	0.071510	0.136250	0.003980	853	120	838	32	823	23	98%	0.23
1403-13	0.069100	0.002910	1.331060	0.057840	0.138100	0.004430	902	89	859	25	834	25	96%	0.12
1403-14	0.067310	0.002870	1.289490	0.054860	0.136940	0.004100	847	91	841	24	827	23	98%	0.10
1403-15	0.071780	0.003150	1.362270	0.060410	0.137590	0.003940	980	92	873	26	831	22	95%	0.14
1403-16	0.067260	0.003760	1.288130	0.069470	0.137630	0.004110	846	119	840	31	831	23	98%	0.13
1403-17	0.067700	0.004320	1.298600	0.072250	0.138830	0.005520	859	136	845	32	838	31	99%	0.26
1403-18	0.066130	0.002690	1.280030	0.061390	0.136630	0.004410	811	87	837	27	826	25	98%	0.09
1403-19	0.068080	0.003100	1.317510	0.066380	0.137140	0.003870	871	97	853	29	828	22	97%	0.07
1403-20	0.067920	0.003200	1.305320	0.061680	0.137340	0.004730	866	100	848	27	830	27	97%	0.35
1403-21	0.075510	0.002170	1.759020	0.067910	0.166670	0.003440	1082	59	1030	25	994	19	96%	0.29
1403-22	0.066880	0.002100	1.280900	0.037410	0.138870	0.004890	834	67	837	17	838	28	99%	0.38
1403-23	0.064280	0.001230	1.228120	0.025780	0.138060	0.001820	751	41	813	12	834	10	97%	0.16
1403-24	0.066260	0.001240	1.264570	0.024970	0.137730	0.001430	814	40	830	11	832	8	99%	0.16
1403-25	0.064920	0.001130	1.234900	0.023080	0.137450	0.001570	772	37	817	10	830	9	98%	0.28
1403-26	0.066510	0.001570	1.263570	0.032670	0.136920	0.002160	823	50	830	15	827	12	99%	0.40
1403-27	0.065110	0.001150	1.235710	0.023980	0.137220	0.001770	778	38	817	11	829	10	98%	0.27
1403-28	0.068180	0.001240	1.297320	0.027110	0.137290	0.001830	874	38	845	12	829	10	98%	0.17
1403-29	0.066420	0.001390	1.260180	0.026490	0.137220	0.001740	820	45	828	12	829	10	99%	0.35
1403-30	0.066360	0.001400	1.263390	0.030910	0.137100	0.002120	818	45	829	14	828	12	99%	0.13
1403-32	0.081160	0.001730	2.164630	0.065780	0.190400	0.003860	1225	43	1170	21	1124	21	95%	0.09
1403-33	0.065520	0.001120	1.251830	0.022610	0.137720	0.001410	791	37	824	10	832	8	99%	0.20
1403-34	0.067610	0.001640	1.291380	0.031480	0.138000	0.002000	857	52	842	14	833	11	98%	0.63
1403-35	0.066110	0.001870	1.252750	0.034960	0.136620	0.002290	810	61	825	16	826	13	99%	0.16
1403-36	0.082480	0.001110	1.993340	0.031100	0.173880	0.001790	1257	27	1113	11	1033	10	92%	0.21
1403-38	0.066920	0.001180	1.276980	0.023200	0.137420	0.001390	835	38	836	10	830	8	99%	0.20
1403-39	0.067410	0.001330	1.284140	0.027110	0.137860	0.001900	850	42	839	12	833	11	99%	0.24
1403-40	0.066030	0.001230	1.266980	0.029430	0.137720	0.001930	807	40	831	13	832	11	99%	0.21

Sample B13 (2024)														
2024-1	0.065500	0.001820	1.261080	0.031570	0.137580	0.002020	790	60	828	14	831	11	99%	0.76
2024-3	0.065550	0.001510	1.261460	0.026960	0.137480	0.001770	792	49	829	12	830	10	99%	0.67
2024-4	0.073800	0.002260	1.639830	0.072270	0.157100	0.004300	1036	63	986	28	941	24	95%	0.43
2024-5	0.065770	0.001710	1.267560	0.031720	0.137710	0.001680	799	56	831	14	832	10	99%	0.17
2024-6	0.065610	0.001510	1.259910	0.028700	0.137160	0.001600	794	49	828	13	829	9	99%	0.10
2024-7	0.192840	0.003750	14.152860	0.272140	0.524830	0.006440	2767	33	2760	18	2720	27	98%	0.58
2024-8	0.125120	0.002920	6.523570	0.256130	0.369490	0.011220	2031	42	2049	35	2027	53	98%	0.15
2024-9	0.066640	0.002420	1.262060	0.033830	0.136860	0.003020	826	78	829	15	827	17	99%	0.95
2024-10	0.064080	0.002440	1.226520	0.048880	0.137390	0.002520	744	82	813	22	830	14	97%	0.52
2024-11	0.066140	0.001880	1.265900	0.036240	0.137420	0.001960	811	61	831	16	830	11	99%	0.75
2024-12	0.065710	0.001680	1.256240	0.032880	0.137210	0.001760	797	55	826	15	829	10	99%	0.34
2024-13	0.065450	0.002010	1.244370	0.040780	0.137260	0.003110	789	66	821	18	829	18	98%	0.23
2024-14	0.091810	0.001810	3.232250	0.095010	0.251450	0.005490	1463	38	1465	23	1446	28	98%	0.51
2024-15	0.187020	0.003180	13.625470	0.269200	0.522990	0.007150	2716	29	2724	19	2712	30	99%	0.50
2024-16	0.065920	0.001250	1.258770	0.026960	0.137290	0.001960	804	41	827	12	829	11	99%	0.08
2024-17	0.066710	0.001660	1.268090	0.031020	0.137130	0.001730	829	53	832	14	828	10	99%	1.35
2024-18	0.067360	0.001430	1.282690	0.031340	0.137190	0.002020	849	45	838	14	829	11	98%	0.57
2024-19	0.064720	0.001490	1.233740	0.029890	0.137480	0.001960	765	50	816	14	830	11	98%	0.12
2024-20	0.065460	0.003630	1.233810	0.066950	0.137320	0.004120	789	120	816	30	829	23	98%	0.51
2024-21	0.066630	0.001730	1.265260	0.031050	0.137180	0.001890	826	56	830	14	829	11	99%	0.05
2024-22	0.074260	0.001500	1.810960	0.043730	0.175420	0.002570	1049	42	1049	16	1042	14	99%	0.55
2024-23	0.066190	0.001590	1.261210	0.030780	0.137450	0.001900	812	51	828	14	830	11	99%	0.30
2024-24	0.067000	0.001230	1.272010	0.026520	0.137150	0.002160	838	39	833	12	829	12	99%	0.25
2024-25	0.102110	0.001800	3.584060	0.079520	0.252520	0.003850	1663	33	1546	18	1451	20	93%	0.37
2024-26	0.064560	0.001480	1.226440	0.028060	0.137150	0.001550	760	50	813	13	829	9	98%	0.27
2024-27	0.067460	0.001500	1.278110	0.027800	0.137070	0.001560	852	47	836	12	828	9	99%	0.99
2024-28	0.091880	0.001830	3.249860	0.102580	0.249300	0.005470	1465	39	1469	25	1435	28	97%	0.30
2024-29	0.066310	0.001830	1.262900	0.030630	0.137480	0.002490	816	59	829	14	830	14	99%	0.16
2024-30	0.103270	0.002060	4.121880	0.093960	0.287030	0.004180	1684	38	1659	19	1627	21	98%	0.38
2024-32	0.165130	0.002750	9.749940	0.164700	0.425100	0.004890	2509	29	2411	16	2284	22	94%	0.27
2024-34	0.087950	0.001420	2.597700	0.041920	0.213070	0.002220	1381	32	1300	12	1245	12	95%	0.61
2024-35	0.067390	0.001930	1.332540	0.039080	0.142400	0.001570	850	61	860	17	858	9	99%	0.32
2024-36	0.073230	0.001920	1.663310	0.045930	0.163620	0.002090	1020	54	995	18	977	12	98%	0.13
2024-37	0.073210	0.001140	1.704990	0.038310	0.167600	0.003010	1020	32	1010	14	999	17	98%	0.74
2024-38	0.070540	0.001670	1.341650	0.030980	0.137440	0.001650	944	50	864	13	830	9	96%	0.35
2024-39	0.066290	0.001430	1.262510	0.028690	0.137480	0.001860	816	46	829	13	830	11	99%	0.48
2024-40	0.069440	0.001550	1.318220	0.034040	0.136960	0.002750	912	47	854	15	827	16	96%	0.37

Table 2. LA-MC-ICP-MS zircon Lu-Hf isotopic data for the granite sample from the Sanfang pluton

Sample	*176Yb/177Hf*	*2σ*	*176Lu/177Hf*	*2σ*	*176Hf/177Hf*	*2σ*	*εHf(t)*	*εHf(0)*	*Age(Ma)*	*TDM1(Ma)*	*TDM2(Ma)*	*f(Lu/Hf)*
Sample A37 (1403)												
1403-01.xls	0.069465	0.001329	0.002551	0.000049	0.282182	0.000018	-4.26	-20.85	815	1573	1977	-0.92
1403-02.xls	0.033276	0.002444	0.001317	0.000096	0.282133	0.000017	-5.35	-22.59	814	1591	2046	-0.96
1403-03.xls	0.052056	0.000445	0.001897	0.000020	0.282240	0.000019	-1.89	-18.82	814	1464	1828	-0.94
1403-05.xls	0.020281	0.000170	0.000823	0.000008	0.282080	0.000013	-6.79	-24.48	823	1645	2143	-0.98
1403-07.xls	0.061695	0.001249	0.002307	0.000047	0.282159	0.000038	-4.69	-21.68	828	1597	2014	-0.93
1403-10.xls	0.035740	0.000612	0.001399	0.000023	0.282159	0.000012	-4.33	-21.68	821	1558	1987	-0.96
1403-11.xls	0.015152	0.000361	0.000611	0.000014	0.282152	0.000011	-3.99	-21.94	829	1536	1971	-0.98
1403-12.xls	0.032853	0.000245	0.001274	0.000009	0.282167	0.000014	-3.95	-21.40	823	1542	1964	-0.96
1403-13.xls	0.060701	0.001586	0.002274	0.000052	0.282210	0.000017	-2.74	-19.88	834	1522	1896	-0.93
1403-14.xls	0.033084	0.001351	0.001302	0.000052	0.282124	0.000017	-5.39	-22.92	827	1603	2058	-0.96
1403-16.xls	0.031782	0.000622	0.001255	0.000024	0.282096	0.000014	-6.26	-23.89	831	1640	2116	-0.96
1403-17.xls	0.034896	0.000528	0.001431	0.000019	0.282118	0.000016	-5.43	-23.12	838	1617	2069	-0.96
1403-18.xls	0.018821	0.001017	0.000813	0.000046	0.281955	0.000025	-11.15	-28.91	826	1817	2418	-0.98
1403-19.xls	0.069655	0.001338	0.002645	0.000045	0.282206	0.000014	-3.22	-20.03	828	1544	1922	-0.92
1403-20.xls	0.043510	0.000604	0.001756	0.000024	0.282195	0.000019	-3.07	-20.41	830	1522	1914	-0.95
1403-22.xls	0.028666	0.000751	0.001136	0.000029	0.282155	0.000015	-3.96	-21.81	838	1553	1976	-0.97
1403-23.xls	0.060435	0.001617	0.002269	0.000057	0.282119	0.000015	-5.96	-23.10	834	1653	2099	-0.93
1403-24.xls	0.040540	0.001049	0.001561	0.000038	0.282197	0.000024	-2.84	-20.33	832	1511	1901	-0.95
1403-26.xls	0.033645	0.000740	0.001340	0.000028	0.282199	0.000015	-2.74	-20.25	827	1499	1891	-0.96

Table 3. Sampling sites and site-mean AMS measurement results for the Sanfang-Yuanbaoshan plutons

Site	*Geographic coordinates*	*Alt.(m)*	*n*	*Km (10^{-6}SI)*	P_J	*T*	*Site mean AMS results*			
							K1	*α95(max/min)*	*K3*	*α95(max/min)*
							Dec (°)/Inc(°)	*(°)*	*Dec (°)/Inc(°)*	*(°)*
Sanfang										
A02	N25°36.269′ E108°46.973′	547	8	40.2	1.017	0.178	155.1/17.4	61.2/35.7	259.7/38.6	47.4/39.1
A04	N25°35.191′ E108°46.424′	680	6	27.5	1.074	0.007	159.2/10.1	28.2/15.6	263.1/53.5	17.6/12.7
A15	N25°22.597′ E108°49.759′	860	6	81.6	1.104	0.776	263.0/43.0	42/4.7	58.9/44.3	11.8/4.3
A20	N25°24.531′ E108°46.455′	1330	6	33.0	1.130	0.377	255.2/18.9	34.5/16.1	48.8/69.1	26.1/12.8
A26	N25°17.328′ E108°44.369′	402	6	76.9	1.083	0.000	223.2/61.7	8.7/5.4	56.9/27.6	16.5/6.2
A31	N25°13.954′ E108°40.646′	770	6	90.5	1.041	-0.155	83.9/42.4	29.7/15.0	292.0/44.0	36.5/12.5
A33	N25°13′ 14.7" E108°51′ 33.4"	293	8	47.9	1.117	0.054	304.4/0.9	62.3/32.7	34.8/24.3	54.2/25.3
A34	N25°17′ 08.1" E108°53′ 10.3"	263	6	52.5	1.022	-0.384	78.6/0.9	6.6/4.8	346.3/68.4	37.4/3.9
A35	N25°17′ 24.0" E108°52′ 26.8"	715	6	55.2	1.063	0.417	251.6/19.7	11.0/4.7	46.5/68.4	11.6/7.6
A36	N25°17′ 44.6" E108°51′ 38.9"	705	6	88.1	1.081	0.392	262.1/21.2	19.1/7.0	40.7/62.7	19/7.9
A37	N25°18′ 45.8" E108°50′ 34.5"	724	6	67.8	1.099	0.148	256.9/14.5	7.9/4.9	54.3/74.3	11.0/3.1
A38	N25°26′ 07.7" E108°48′ 50.7"	1153	7	42.6	1.140	0.737	263.9/36.6	14.7/4.9	86.4/53.4	10.1/4.7
A40	N25°22′ 52.5" E108°54′ 03.7"	772	7	48.9	1.071	0.649	289.5/13.2	23.2/5.3	58.1/69.4	6.9/4.1
A41	N25°22′ 24.9" E108°53′ 38.4"	674	6	46.9	1.059	0.569	264.2/20.8	17.3/2.6	44.9/63.9	7.3/2.6
A42	N25°21′ 49.1" E108°52′ 57.9"	636	6	57.5	1.071	0.722	216.8/26.1	26.6/7.7	33.1/63.9	10.4/7.7
A43	N25°20′ 43.1" E108°50′ 39.9"	993	7	99.5	1.083	0.562	265.4/23.0	16.4/4.5	76.2/66.7	6.7/4.4
A44	N25°27′ 23.2" E108°50′ 42.3"	1085	7	100.0	1.116	0.687	253.3/14.8	15.7/9.1	91.6/74.4	10.3/5.5
A45	N25°28′ 15.0" E108°51′ 27.9"	1001	6	109.0	1.156	0.912	224.1/1.4	37.8/3.7	30.7/88.6	7.4/0.6
A46	N25°23′ 25.3" E108°49′ 03.4"	983	8	88.8	1.097	0.671	253.1/20.8	13.2/6.4	61.4/68.8	7.9/4.2
A47	N25°25′ 51.6" E108°44′ 30.3"	1196	7	93.3	1.071	0.776	210.7/53.0	27.3/5.8	95.3/17.9	8.0/4.1
A48	N25°28′ 29.2" E108°43′ 21.2"	788	8	46.6	1.042	-0.111	163.0/31.9	10.8/2.9	302.6/50.7	17.9/2.5
A49	N25°29′ 45.9" E108°43′ 24.5"	704	8	55.5	1.055	-0.221	173.5/19.8	4.6/2.1	276.5/32.1	12.2/4.0
A51	N25°32′ 04.4" E108°43′ 51.3"	566	6	50.3	1.067	-0.282	150.8/14.4	4.1/2.3	264.5/57.3	12.0/3.2
A52	N25°31′ 10.6" E108°43′ 39.7"	612	6	44.0	1.030	-0.065	3.5/10.2	9.4/4.4	261.2/49.8	18.0/5.1
A53	N25°21′ 09.7" E108°53′ 37.2"	677	6	41.9	1.066	0.725	166.0/32.7	19.9/9.0	355.4/56.9	10.1/3.7
A54	N25°15′ 25.5" E108°51′ 46.0"	296	6	74.4	1.022	0.193	306.7/6.9	67.3/6.6	45.8/52.6	13.8/7.0
A55	N25°15′ 52.1" E108°45′ 18.9"	317	6	124.0	1.062	0.413	245.2/36.5	22.3/6.8	87.8/51.3	8.0/6.9
A56	N25°15′ 03.6" E108°45′ 05.5"	353	6	66.8	1.037	0.161	304.1/26.4	35.2/9.9	89.6/58.9	14.8/11.8
A57	N25°12′ 51.7" E108°45′ 04.4"	630	5	57.3	1.042	0.071	292.5/42.4	16.1/7.1	91.9/45.7	16.2/7.1
A58	N25°13′ 36.6" E108°44′ 15.8"	426	6	91.6	1.043	-0.073	264.2/48.0	17.4/6.9	112.2/38.5	25.3/8.5
A59	N25°17′ 32.8" E108°43′ 37.6"	441	6	96.2	1.028	0.104	243.1/38.8	21.8/6.7	115.4/37.3	25.5/10.2
A60	N25°19′ 20.4" E108°41′ 58.6"	870	6	41.9	1.026	0.268	49.1/44.1	68.8/10.6	289.8/26.8	16.1/8.5
A61	N25°20′ 23.1" E108°42′ 24.2"	940	7	133.0	1.038	0.460	172.1/55.1	18.1/5.2	278.2/11.0	18.0/3.7
A63	N25°16′ 04.1" E108°41′ 01.9"	533	7	112.0	1.038	0.128	122.9/53.3	18.6/7.2	298.1/36.6	12.0/5.2
A65	N25°14′ 17.1" E108°40′ 46.5"	722	8	107.0	1.030	-0.178	161.9/42.6	67.4/11.4	310.7/43.0	17.9/11.2
Yuanbaoshan										
B01	N25°24′ 11.4" E109°06′ 22.4"	494	7	108.0	1.079	0.390	274.4/11.5	16.1/4.4	36.0/68.8	17.3/4.7
B02	N25°24′ 00.0" E109°06′ 18.9"	489	5	32.7	1.026	0.361	101.2/6.3	34.0/13.8	5.8/40.7	21.1/10.3
B03	N25°24′ 30.1" E109°06′ 51.7"	514	6	135.0	1.064	0.464	112.8/2.0	13.5/5.9	19.0/62.8	7.6/5.1

B04	N25°25′ 09.4" E109°07′ 23.8"	575	5	108.0	1.068	0.083	313.5/1.3	42.4/6.4	220.9/64.0	38.8/4.0
B05	N25°25′ 43.0" E109°08′ 29.0"	715	6	76.4	1.128	0.643	128.1/2.6	32.4/3.7	249.7/85.0	20.5/3.8
B06	N25°26′ 11.6" E109°08′ 24.6"	828	6	172.0	1.041	0.479	148.5/4.1	26.7/4.3	326.5/85.9	10.7/4.3
B07	N25°27′ 34.9" E109°09′ 56.5"	986	7	112.0	1.150	0.775	318.9/2.9	15.4/1.6	71.1/82.3	3.7/1.5
B08	N25°28′ 18.0" E109°10′ 32.0"	802	6	197.0	1.168	0.817	336.0/3.2	24.0/9.5	114.9/85.7	10.9/3.7
B09	N25°28′ 47.3" E109°10′ 47.6"	622	6	82.9	1.078	-0.149	167.6/6.9	7.8/5.4	34.0/80.1	16.4/6.2
B10	N25°29′ 41.9" E109°12′ 03.7"	332	6	74.2	1.102	-0.384	333.0/7.4	7.3/1.7	71.6/48.7	22.7/6.8
B11	N25°15′ 13.7" E109°10′ 29.8"	173	6	79.7	1.009	0.166	255.3/58.8	58.1/18.9	159.5/3.2	46.7/18.8
B12	N25°17′ 24.2" E109°11′ 45.9"	202	8	167.0	1.016	-0.094	165.0/17.7	27.5/18.6	282.4/55.3	43.4/18.5
B13	N25°18′ 06.9" E109°11′ 52.2"	222	6	152.0	1.023	-0.325	155.9/23.4	16.9/12.4	262.5/33.4	48.7/15.3
B14	N25°19′ 08.4" E109°11′ 46.9"	234	6	135.0	1.034	-0.305	155.4/24.6	13/3.4	8.9/61.3	31.6/10.5
B15	N25°20′ 35.0" E109°12′ 26.6"	315	6	74.0	1.026	-0.094	165.5/12.6	14.0/3	258.8/14.4	26.7/6.8
B16	N25°21′ 03.0" E109°11′ 38.0"	523	5	85.9	1.038	0.534	181.2/30.4	19.7/11.8	70.5/31.1	21.4/6.6
B17	N25°21′ 46.0" E109°10′ 43.3"	837	8	76.3	1.056	0.127	182/28.5	26.1/6.5	78.5/23.2	33.7/6.8
B18	N25°16′ 45.0" E109°12′ 38.5"	175	6	83.6	1.022	-0.265	131.6/8.3	14.8/5.7	38.1/22.9	18.8/13.9
B19	N25°18′ 12.6" E109°13′ 29.7"	329	7	63.0	1.028	-0.235	184.9/27.2	18.1/5.7	42.5/57	8.8/4.8
B20	N25°25′ 02.7" E109°12′ 54.6"	785	6	79.3	1.172	0.636	269.7/36.4	10.5/4.1	94.4/53.5	5.9/1.2

Note: Alt.: Altitude, n: number of specimen at sampling site, Km: bulk magnetic susceptibility PJ: degree of susceptibility anisotropy, T: shape parameter of the AMS ellipsoid, K1: Magnetic lineation, K3: The pole of the magnetic foliation, Inc.: Inclination, Dec.: Declination, α95 (max/min): the long and short axes of the confidence ellipsoid at 95% level

954

Table 4. The density of the Sanfang-Yuanbaoshan granites and country rocks

Strata/Rock	*Lithology*	*Sampling number*	*Density of each sample (g/cm^3)*	*Average of measured density (g/cm3)*	*Standard derivation*
γ2 Sanfang	Granite	1404	2.630	2.606	0.0425
		A35	2.534		
		A37	2.586		
		A38	2.601		
		A39	2.663		
		A40	2.549		
		A42	2.559		
		A45	2.670		
		A46	2.671		
		A48	2.592		
		A49	2.615		
		A51	2.591		
		A52	2.622		
		A55	2.673		
		A57	2.576		
		A58	2.648		
		A59	2.534		
		A62	2.582		
		A63	2.631		
		A65	2.602		
		A66	2.587		
γ2 Yuanbaoshan	Granite	B07	2.597	2.606	0.0129
		B09	2.594		
		B02	2.621		
		B05	2.623		
		B19	2.591		
		B20	2.612		
Sibao Group	Slate	1406	2.741	2.678	0.0577
	Slate	1415	2.673		
	Slate	1419	2.664		
	Slate	1422	2.757		
	Slate	1425	2.740		
	Sandstone	1427	2.648		
	Sandstone	1429	2.684		
	Slate	1439	2.706		
	Slate	1447	2.679		
	Slate	1451	2.622		
	Sandstone	1453	2.763		
	Sandstone	1458	2.568		
	Slate	1459	2.763		

	Slate	1460	2.681		
	Slate	1468a	2.692		
	Slate	1469	2.754		
	Slate	2002	2.696		
	Slate	2003	2.601		
	Sandstone	2004	2.671		
	Sandstone	2006	2.545		
	Sandstone	2007	2.655		
	Sandstone	2020	2.628		
	Slate	2031	2.678		
	Slate	2051	2.584		
	Slate	2052	2.700		
	Slate	2054	2.722		
	Slate	2055	2.685		
Danzhou Group	Sandstone	1420	2.756	2.686	0.0851
	Sandstone	1461	2.734		
	Sandstone	2000-1	2.528		
	Sandstone	2001	2.738		
	Sandstone	2064	2.704		
	Blastopsammite	2066	2.585		
	Sandstone	2067	2.759		
Sinian	Sandstone	2040	2.715	2.710	0.0066
		2040-1	2.714		
		2040-2	2.701		